



**TECHNISCHE
UNIVERSITÄT
WIEN**

Vienna University of Technology

Unterschrift des Betreuers

DIPLOMARBEIT

Segmentation Algorithms for Quantitative Analysis of Functional OCT Data

ausgeführt am Institut für Angewandte Physik
der Fakultät für Physik der Technischen Universität Wien

unter der Anleitung von

Ao. Univ.-Prof. Dr. Martin Gröschl

in Zusammenarbeit mit der Medizinischen Universität Wien

unter der Betreuung von

Ao. Univ.-Prof. Dr. Rainer A. Leitgeb

durch

Michael Unterluggauer, BSc

Josefstraße 64/6, 3100 Sankt Pölten

Datum

Unterschrift (Student)

Abstract

Functional optical coherence tomography (OCT) provides intrinsic tissue contrast that yields important information about tissue physiology and dynamics. In particular, OCT Angiography and Doppler OCT provide vascular structure without the need of contrast agents together with the quantitative information on blood flow. However, quantitative data on vascular density and flow critically depend on the proper segmentation of the structures of interest.

The aim of the thesis was the adaption and further refinement of segmentation algorithms to analyze OCT angiography data. Particular structures were the retinal nerve fiber layer as well as capillary layers within the neural retina. The performance of the algorithm was tested on healthy in-vivo data as well as on images of different retinal pathologies. For this thesis the retinal layer segmentation was acquired along with an optic nerve head segmentation and a vessel segmentation. Furthermore, microvascular perfusion parameters were defined and calculated.

Kurzfassung

Mittels funktioneller optischer Kohärenztomografie (OCT) erhält man intrinsischen Gewebs-Kontrast durch welchen wichtige Informationen über Gewebspathologie und dessen Dynamik gewonnen werden können. Im Speziellen werden vaskuläre Strukturen und quantitative Informationen über den Blutfluss mit Hilfe von OCT Angiographie und Doppler OCT erlangt, ohne dabei Kontrastmittel verwenden zu müssen. Quantitative Daten über die Gefäßdichte und Durchblutung hängen jedoch kritisch von einer funktionierenden Segmentierung der zu untersuchenden Strukturen ab.

Das Ziel dieser Arbeit war die Adaption und Verbesserung von Segmentierungsalgorithmen, die die Analyse von OCT Angiographie Daten ermöglichen. Bei den Strukturen die näher untersucht wurden, handelt es sich um die Nervenfaserschicht und die Kapillarschichten der Retina. Der Algorithmus wurde einerseits anhand von gesunden in-vivo Daten und andererseits anhand von Bildern verschiedener retinalen Pathologien getestet. Für diese Arbeit wurden ein Segmentierungsalgorithmus für die retinalen Schichten, sowie eine Segmentierung des Sehnervs und der Blutgefäße erarbeitet. Außerdem wurden mikrovaskuläre Durchblutungsparameter definiert und berechnet.

Table of Contents

1	Introduction	1
2	Basics	5
2.1	Physics	6
2.1.1	Optical Coherence Tomography	6
2.1.2	Interferometer	11
2.1.3	Resolution	16
2.1.4	Angiography	17
2.2	Medical Image Processing	18
2.2.1	Shortest Path Problem	19
2.2.2	Clustering	20
2.2.3	Image Registration	21
2.3	The Human Eye	21
3	Methodology	26
3.1	Workflow	26
3.2	OCT	27
3.2.1	OCT System Setup	27
3.2.2	Swept Source OCT	28
3.2.3	Remapping	30
3.3	Image Processing	31
3.3.1	Image Registration	32
3.3.2	Retinal Layer Detection	33
3.3.3	Optic Nerve Head Segmentation	35
3.3.4	Major Vessel Segmentation	35
3.3.5	Microvasculature Perfusion Parameters	36
4	Results and Discussion	39
4.1	Image Registration	39
4.2	ONH Segmentation	40
4.3	Retinal Layer Segmentation	41
4.4	Major Vessel Segmentation	45
4.5	Retinal Perfusion	46
4.5.1	Comparison of NFL-thickness and retinal perfusion research study	46
4.5.2	Retinal Oxygen Saturation and Microvascular Hemodynamic Parameters research study	49
5	Conclusion	51
6	Outlook	53

References	55
List of figures	57
List of tables	58
List of equations	59

Abbreviations

OCT	Optical Coherence Tomography
TD-OCT	Time Domain OCT
FD-OCT	Fourier Domain OCT
SD-OCT	Spectral Domain OCT
SS-OCT	Swept Source OCT
FFT	Fast Fourier Transformation
FWHM	Full width at half maximum
PSF	Point spread function
NFL	Nerve fiber layer
GCL	Ganglion cell layer
RPE	Retinal pigment epithelium
IS	Inner segment
OS	Outer segment
SNR	Signal to noise ratio
FOV	Field of View

1 Introduction

In today's medicine, it is of great importance to acquire as much information on the human body as possible. For this purpose, methods are being developed to improve the resolution and the quality of imaging devices. An improved image quality does not only help diagnosing a disease but also helps following and understanding the process of the disease better. Another important issue is the discovery of so-called biomarkers, which are measurable indicators for diseases. Ideally, a biomarker can be found that gives hints about a disease before any significant damage is done, in which case reasonable countermeasures can be initiated.

The improved imaging methods also demand higher-quality processing and evaluation of the data. Due to the improved resolution of the recorded medical images, the required disk space is increasing. Additionally, a great number of patients has to be imaged in medical research studies to calculate significant statistical evidence on possible biomarkers. To deal with the huge amount of data and to prevent a flooding of the servers with non-utilized data, a fast processing of the measured raw data is mandatory. Furthermore, analyzing a huge amount of data by hand is too time-consuming. This shows the importance of programming image processing algorithms, that are as automatized as possible.

The main focus of this thesis lies on programming algorithms for processing images of the retina of human eyes in order to eventually gain perfusion parameters of the retina. These images were recorded with the help of Optical Coherence Tomography (OCT), which is an imaging technique that is based on low-coherence interferometry. OCT is especially used in ophthalmology, since it is non-invasive and a full 3D tomogram can be gathered. A very good method for detecting the vessel structures of the retina is retinal angiography.

Before the perfusion parameters of the retina can be calculated, several steps have to be taken. First of all, the raw data measured with the help of OCT have to be processed in order to get the 3D angiography and the images from the 100kHz¹ acquisition of the retina. Afterwards, a segmentation algorithm is used on the 100kHz data to receive the different retinal layers. This algorithm is based on solving a shortest path problem by minimizing a gradient-based cost function. The segmentation of the different retinal layers is important in order to be able to calculate only the perfusion parameters for the layers that are desired in the research studies. The gained retinal layers can be easily transferred onto the corresponding angiography. Furthermore, algorithms for the segmentation of the optical nerve head and the major vessels within the retina are developed. When excluding them from the angiography of the OCT, the microvascular structures remain. Thereby, the perfusion parameters can be calculated for the retinal microvascular structure. In **chapter 2**, the physical background that is needed for understanding OCT and how the images are obtained is described. Furthermore, the basic principles of the

¹100kHz refers to the A-scan rate of the OCT system (see chapter 3.2.2).

used image processing methods are explained. Finally a short introduction in the relevant anatomical and pathological aspects of the human eye is given. **Chapter 3** describes the setup of the OCT system used for the imaging in detail. The image processing theory, which is necessary for the implementation, can be found in this chapter as well. While **chapter 4** gives an overview of the results on the coded image processing algorithm, **chapter 5** gives a conclusion and **chapter 6** an outlook.

The calculations of the perfusion parameters already build the basis for different medical research studies. Laurin Ginner has constructed the OCT system with which the images were recorded. Furthermore, he was in charge of measuring the patients of the research studies.

Einleitung

In der heutigen Medizin ist es sehr wichtig, so viele Informationen wie möglich über den menschlichen Körper zu erhalten. Zu diesem Zweck wird stets an neuen Methoden gearbeitet, um bessere Abbildungsverfahren mit höherer Auflösung und Qualität zu entwickeln. Dies hilft nicht nur die Diagnose von Krankheiten zu vereinfachen, sondern auch den Verlauf einer Krankheit besser verstehen und verfolgen zu können. Ein weiterer wichtiger Punkt ist das Erkennen und Auffinden von Biomarkern aus diesen Abbildungen, welche als Indikatoren für Krankheiten dienen. Bestenfalls können Biomarker gefunden werden, die Hinweise auf eine Krankheit geben bevor ein signifikanter Schaden angerichtet wurde. In diesem Fall können angemessene Gegenmaßnahmen initiiert werden.

Die verbesserten Abbildungsverfahren stellen auch höhere Anforderungen an die Verarbeitung und Auswertung der Daten. So wird durch die immer hoch auflösenderen Bilder immer mehr Speicherplatz für die gemessenen Daten benötigt. Außerdem muss bei einer medizinischen Studie eine Vielzahl an Patienten gemessen werden, um eine signifikante Statistik über mögliche Biomarker zu erhalten. Damit die Server nicht mit nicht ausgewertetem Bildmaterial überlaufen, ist es wichtig, die gemessenen Rohdaten schnell weiterzuverarbeiten. Außerdem ist die manuelle Auswertung von großen Datenmengen sehr zeitaufwändig. Dies zeigt die Wichtigkeit Algorithmen für die Bildverarbeitung neu zu entwickeln, welche die Bildmaterialien automatisieren und so rasch wie möglich aufarbeiten.

Der Schwerpunkt dieser Arbeit liegt darin, Algorithmen zur Bildverarbeitung der Retina des menschlichen Auges zu programmieren und daraus Perfusions-Parameter der Retina zu berechnen. Die Bilder wurden mithilfe von Optischer Kohärenztomografie (OCT) aufgenommen, einem Abbildungsverfahren, das auf Interferenz basiert. OCT wird speziell in der Augenheilkunde verwendet, da dieses Verfahren nicht invasiv ist und ein vollständiges 3D-Tomogramm aufgenommen werden kann. Eine sehr gute Methode, um die Gefäßstruktur in der Retina zu detektieren, ist die Angiographie.

Um die Perfusions-Parameter der Retina berechnen zu können, müssen mehrere Arbeitsschritte durchgeführt werden. Zuerst müssen die Rohdaten, welche mit einem OCT aufgenommen wurden, vorverarbeitet werden, um eine 3D-Angiographie und die Bilder der 100kHz² Aufnahme der Retina zu erhalten. Danach wird ein Segmentierungs-Algorithmus auf die 100kHz Daten angewendet, um die verschiedenen Schichten der Retina in den Bilddaten zu erkennen und zu differenzieren. Der Algorithmus basiert auf der Lösung des „kürzesten Pfad“-Problems im Zusammenspiel mit einer Gradient-basierten Kostenfunktion. Die Segmentierung der verschiedenen Schichten der Retina ist die Grundlage, um die Perfusions-Parameter in den Schichten berechnen zu können, die für die medizinischen Studien gewünscht sind. Die so erhaltenen retinalen Schichten können danach auf die zugehörige Angiographie umgerechnet werden. Weiters werden Algorithmen für die Segmentierung des Sehnervs und der großen Blutgefäße innerhalb der Retina entwickelt. Wenn diese aus den Daten der Angiographie entfernt werden, bleibt

²100kHz bezieht sich auf die A-scan Rate des OCT Systems (siehe Kapitel 3.2.2).

nur noch die mikrovaskuläre Struktur über. Auf diese Art und Weise können die Perfusions-Parameter der mikrovaskulären Struktur der Retina berechnet werden. In **Kapitel 2** wird das physikalische Hintergrundwissen beschrieben, welches notwendig ist, um OCT und das Zustandekommen der Bilder zu verstehen. Des Weiteren wird das Grundprinzip der verwendeten Bilderverarbeitungsmethoden erklärt. Am Ende des Kapitels wird noch eine Einleitung in relevante anatomische und pathologische Aspekte des menschlichen Auges gegeben, die im Kontext dieser Arbeit notwendig sind. **Kapitel 3** beschreibt detailliert das Setup des OCT Systems, welches für die Aufnahmen verwendet wurde. Auch die für die Implementierung notwendige Bildverarbeitungstheorie wird in diesem Kapitel erläutert. Während **Kapitel 4** einen Überblick über die Resultate der programmierten Bildverarbeitungsalgorithmen liefert, sind abschließend in **Kapitel 5** ein Fazit und in **Kapitel 6** ein Ausblick der Arbeit zu finden.

Die in dieser Arbeit durchgeführten Berechnungen der Perfusions-Parameter sind bereits Grundlage verschiedener medizinischer Studien. Laurin Ginner hat das OCT System, mit welchem die Bilder aufgenommen wurden, aufgebaut. Weiters war er für die Messung der Patienten für die Studien verantwortlich.

2 Basics

Over the time diverse imaging techniques have been developed. Depending on their resolution and depth penetration as well as their ability to image specific biological tissue, they are used for certain medical fields. Microscopy is used for studying cells or to get a better understanding how diseases work, since it has a high resolution of about $1\text{ }\mu\text{m}$ and below. Since in standard microscopy, light in visible range is used, it has the disadvantage that it is highly scattered. Thus only the surface of a structure is visible. Imaging techniques that use X-rays can be used to show the bone structure of the human body. This is possible because X-rays have a considerably higher penetration depth due to the high energy level of the beam. As a negative side effect, harmful ionization is caused by the X-ray beams. Furthermore, not all structures in the human body -such as organs- are suitable for X-ray imaging techniques. A possibility to record internal structures is provided by ultrasound imaging. Depending on the frequency of the ultrasound waves, it has a resolution of about 15 to $100\text{ }\mu\text{m}$. This resolution isn't sufficient enough for ophthalmology. Another imaging technique that is similar to ultrasound is optical coherence tomography (OCT). However instead of using ultrasound waves, it uses light. With the properties of OCT imaging, it has developed as the leading imaging method for ophthalmology to detect early stages of diseases even before physical symptoms such as an irreversible vision loss occur. Furthermore, disease monitoring can be made to see if the performed treatments are effective. Another application area among many others is, for example, noninvasive imaging of different human skin diseases.

Since the number of imaging techniques as well as their information content are expanding, biomedical image processing becomes very important in order to get access to all the information contained in the image. Biomedical image processing is an interdisciplinary research field attracting not only physicians, but also mathematicians, computer scientists, engineers and biologists. The principle objective of image processing is to process and analyze images in order to get high quality information for disease diagnoses and treatment. Due to expanding imaging possibilities and the higher information content, the automation of the image processing becomes more and more important.

In this chapter, the theoretical basics of the main themes will be treated in detail in order to make the rest of this thesis more easily accessible. It covers not only the physical basics of OCT and the theory of the used image processing algorithms but also a very general overview of the medical aspects.

2.1 Physics

2.1.1 Optical Coherence Tomography

Optical coherence tomography (OCT) is a fast developing imaging technique. The deep interest for OCT originates from the fact that it has unique features that are especially important in biomedical optics and medicine. Not only can tissue pathology be imaged in situ and in real time, but also with good resolutions of $1\text{--}15\mu\text{m}$, which is determined by the coherence length of the light source [5]. So OCT closes the gap between ultrasound and microscopy, as can be seen in figure 2.1. Another great advantage of this imaging technique is that it is a non-invasive procedure, making it more suitable for research studies.

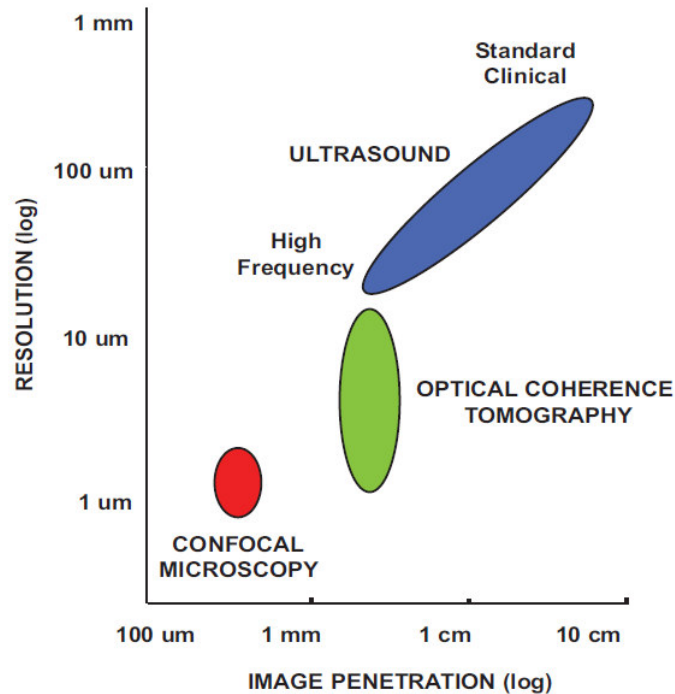


Figure 2.1: Comparison of resolution and imaging depth for ultrasound, OCT and confocal microscopy. OCT has an axial image resolution from $1\text{--}15\mu\text{m}$ [5].

In figure 2.2, a generic OCT system is illustrated. A beam gets emitted from a low-coherence light source. After passing through various optical gadgets, the beam is directed onto the sample. There, the beam is reflected. The reflected beam interferes with a reference beam and is directed to a detector. After various signal processing steps on the computer, the OCT image including depth information of the sample can be observed.

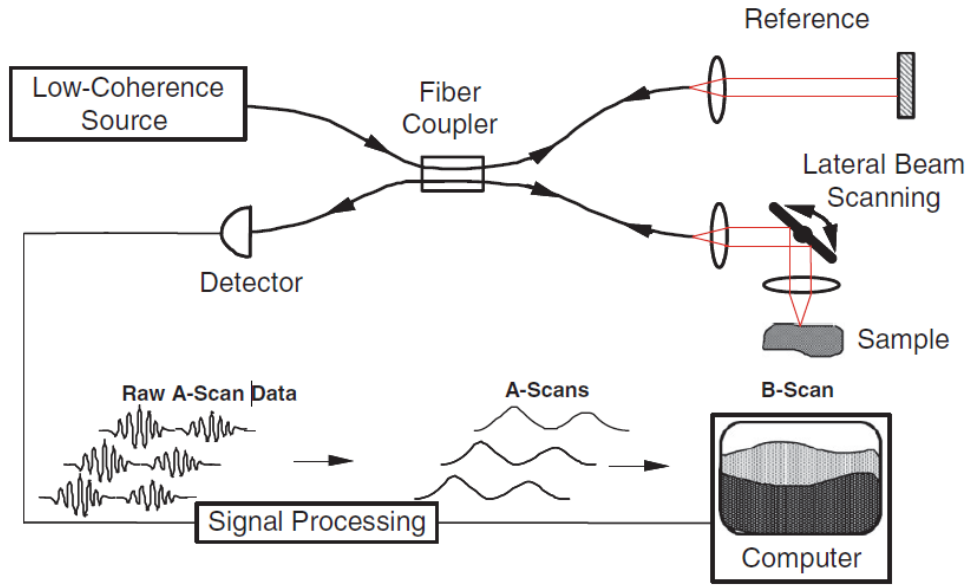


Figure 2.2: Schematic of a generic OCT system [5]

The basic principle of OCT is similar to ultrasound imaging, but while ultrasound imaging uses sound, OCT uses light. Though there are many different ways for performing OCT, the essential imaging is performed by measuring the magnitude and echo time delay of the beam that is backreflected from internal microstructures of the observed tissue. Depending on the optical properties and boundaries between structures, the light beam is backreflected differently. By measuring the ‘echo time’, the dimension of these structures can be determined. Already in 1971, Michel Duguay proposed that optical echoes can be used to see through biological tissue [5]. The echo time is the time it takes for the light beam to be backreflected or backscattered from the different structures at varying axial distances.

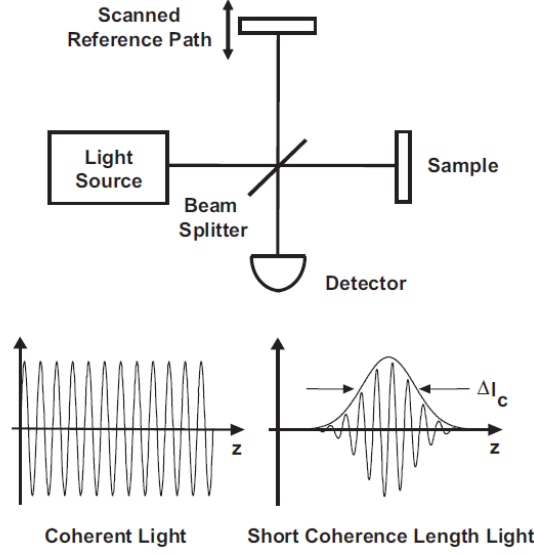


Figure 2.3: Basic principle of low-coherence interferometry [5]

Low-Coherence Interferometry [5]

Since OCT is based on the measurement of the magnitude and echo time delay of backscattered light, a method which measures these parameters with a very high sensitivity is required. An ideal optical measurement technique for this purpose is low-coherence interferometry. The principle of interferometry can be seen in figure 2.3. A light beam is emitted from the light source onto a beam splitter, where it gets divided. From there, one light beam $E_s(t)$ (signal beam) is directed onto the sample and the other beam $E_r(t)$ (reference beam) to the reference path, where the distance the light beam has traveled is known. The backreflected beams from the sample path and reference path interfere and the electric field can be measured at the detector. The measured intensity of the interference is proportional to the square of the total field:

$$I_o \sim |E_r|^2 + |E_s|^2 + 2E_r E_s \cos(2k\Delta L), \quad (2.1)$$

with E_r as reference beam, E_s as signal beam and ΔL as path length difference between the signal and reference arms of the interferometer. For the detection of optical echoes, a light source with low-coherent light is required. To observe interference with low-coherence light, the path lengths of the reference and measurement arms have to be matched within the coherence length of the light. By demodulating the interference signal, the magnitude and echo time delay can be measured. The axial image resolution depends on the coherence length of the used light source.

The depth structure can be calculated from the observed interferogram. The depth information of a single point is called ‘A-scan’ (see figure 2.4 left). With the help of galvo-scanners, the depth information of an area or even a volume can be obtained. If a line scan is performed, the single point depth information of all the A-scans

yields to a 2D image, which is called ‘B-scan’ (see figure 2.4 middle). When a second scanner with a scanning direction perpendicular to the first one is used, a full 3D image of a sample can be obtained (3D-OCT) (see figure 2.4 right).

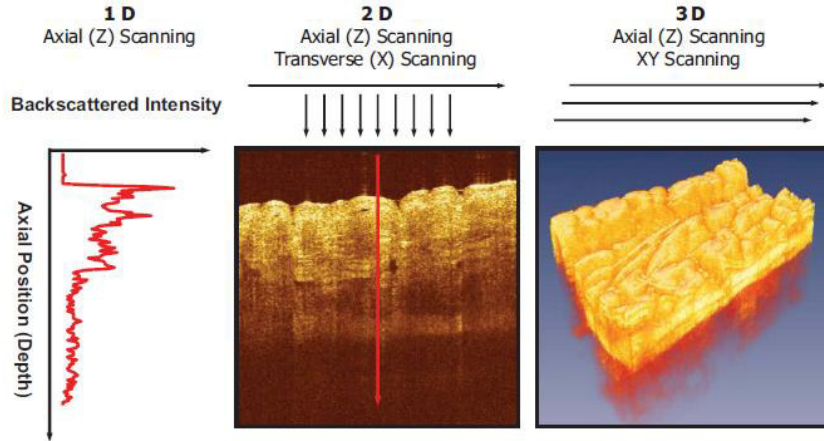


Figure 2.4: An A-scan (left) measures the backreflection versus depth of a single point, while a two-dimensional B-scan (middle) is generated by a series of A-scans at different transverse positions. A three-dimensional data set (right) is gained with a second perpendicular scanner [5].

Because of its benefits, the research on OCT is intense, resulting in various imaging methods with OCT systems. Depending on the way of the measurement domain, there are two main principles of OCT systems, Time Domain OCT and Fourier Domain OCT:

Time Domain OCT (TD-OCT)

Early OCT imaging systems used time domain detection, a method that operates in direct depth-space. An A-scan can be obtained by measuring the interference signal while the reference arm is moved in axial direction at constant speed. With the help of a photodetector, the time delay between the reference and the sample path can be measured. To obtain interference, the path length difference between the backscattered light from the sample and the reference arm light has to be smaller than the coherence length of the light. Since the reference arm has to be moved mechanically, this method is time-consuming, which is an important factor when it comes to in vivo measurements. In TD-OCT only a fraction of the light from the sample that matches the instantaneous delay of the reference beam to within the coherence length can actually contribute to the OCT signal. In addition, the signal SNR critically decreases with reference arm scanning speed and optical bandwidth [13].

Fourier Domain OCT (FD-OCT)

Another possibility to perform the detection is the measurement of the interference spectrum from the reference and sample beam. Hence, this principle operates in the Fourier domain instead of the time domain. When measuring the spectral interference pattern, the depth structure can be determined from the Fourier transformation of the spectra with the help of the Wiener–Khinchin theorem (see equation 2.9).

The Fourier domain detection has a powerful sensitivity advantage over the time domain detection of approximately the ratio of the axial resolution to the axial imaging depth [11]. Furthermore it can measure all the echoes of light simultaneously, which is a great benefit regarding the measuring time (up to 100 times), since no movement in the reference arm is needed. Thus, an A-scan can be measured in a single exposure. Since the measuring time is an important factor for avoiding movement artifacts while doing in vivo measurements, FD-OCT gives a great boost in application possibilities for OCT. A disadvantage of FD-OCT is that more expensive parts (such as fast swept sources or data acquisition electronics) are required.

The FD-OCT can be split into two further detection types, the spectral domain OCT (see figure 2.5 (left)) on the one hand and the swept source OCT (see figure 2.5 (right)) on the other hand:

- Spectral Domain OCT:

In spectral domain OCT (SD-OCT), the detector is replaced with a spectrometer. Furthermore, it uses a broad-bandwidth light source and a line scan camera. With the setup of the SD-OCT, all spectra are gathered at once, which gives a great improvement regarding the measuring time. Another advantage is that the setup is cheaper than e.g. a Swept Source OCT. On the other hand, SD-OCT has the disadvantage of a signal fading or SNR roll-off with increasing depth.

- Swept Source OCT:

The images that are used for this master thesis are recorded with a swept source OCT (SS-OCT). It uses an interferometer with a narrow bandwidth light source that sweeps its frequency in time. With the setup of a SS-OCT, it is possible to record the spectral interference pattern over time and the depth structure with one sweep. In comparison with SD-OCT, the SS-OCT offers a better sensitivity and a lower SNR roll-off with increasing depth. Due to the technical complexity of fast swept sources plus the advanced data acquisition electronics, SS-OCT is still more expensive.

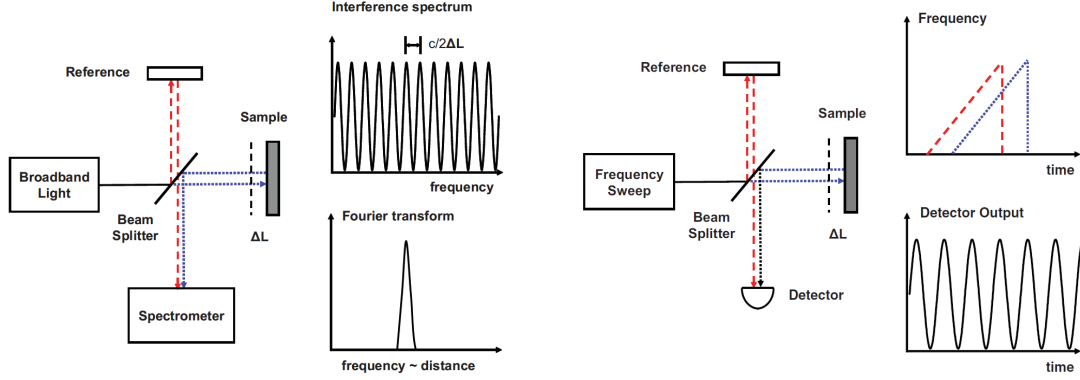


Figure 2.5: Schematics of FD-OCT principles: SD-OCT (left) and SS-OCT (right). The SD-OCT uses a broadband light source and the spectrum of the interference is measured with a spectrometer and a line scan camera. The SS-OCT uses a narrow band, frequency swept laser and detectors [5].

2.1.2 Interferometer

The basic interferometer theory is adapted from [5].

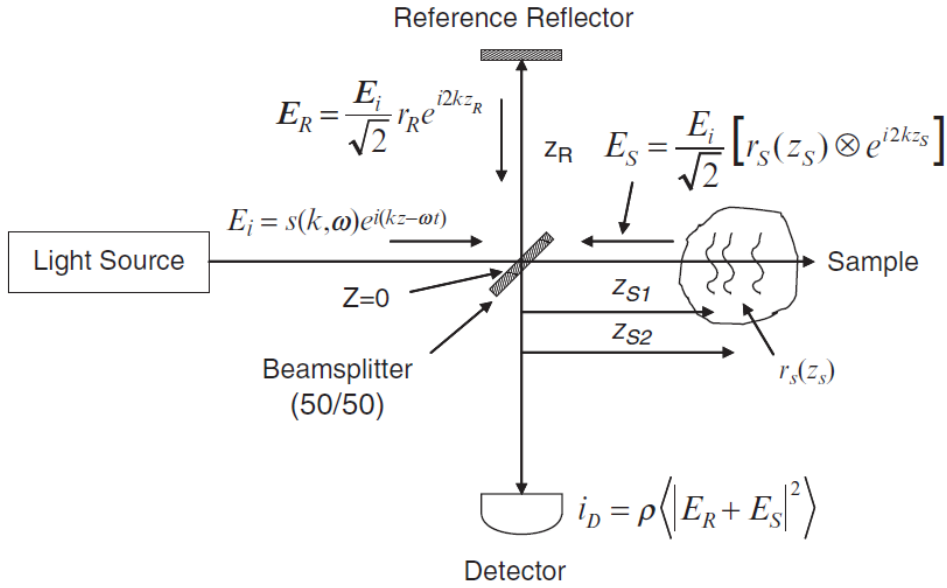


Figure 2.6: Schematic of a Michelson interferometer that is used in OCT [5].

A Michelson Morley interferometer forms the basis of FD-OCT. For the case of SS-OCT, a Mach-Zehnder configuration is usually used due to balanced detection configuration. Figure 2.6 shows a schematic build up of a Michelson interferometer. A light source which illuminates the interferometer with a polychromatic plane wave is used. A polychromatic plane wave E_i can be expressed with equation 2.2.

$$E_i = s(k, \omega)e^{i(kz - \omega t)} \quad (2.2)$$

2. Basics

$s(k, \omega)$ is the electric field amplitude dependent on the wavenumber $k = 2\pi/\lambda$ and the angular frequency $\omega = 2\pi\nu$, t the time and z the optical axis coordinate. The observed sample has a depth-dependent electric field reflectivity along the sample beam axis $r_S(z_S)$. The variable z_S indicates the pathlength between the beamsplitter and the sample arm. Since the refractive index of biological tissue varies continuously, $r_S(z_S)$ is continuous as well.

For a better understanding, we set an illustrative example with N discrete, real delta function reflections of the form

$$r_S(z_S) = \sum_{n=1}^N r_{Sn} \delta(z_S - z_{Sn}), \quad (2.3)$$

with the field reflectivities r_{S1}, r_{S2}, \dots and the pathlengths from the beamsplitter z_{S1}, z_{S2}, \dots , as can be seen in figure 2.7. The power reflectivity is obtained by squaring the magnitude of the electric field reflectivity (e.g. $R_{S1} = |r_{S1}|^2$). The aim of low-coherence interferometry in OCT is to gather the function $\sqrt{R_S(z_S)}$, which gives the correlation between the power reflectivity and the depth coordinate.

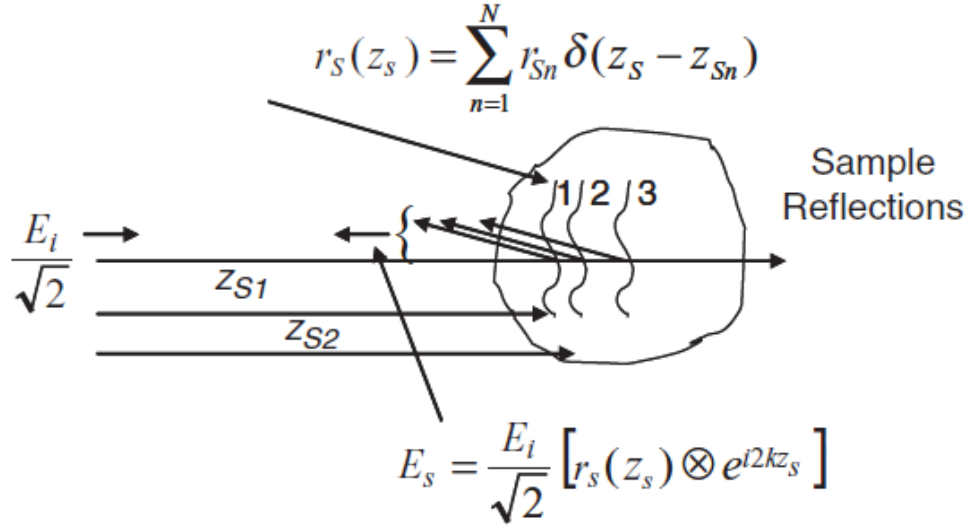


Figure 2.7: Model of a sample with a series of discrete reflectors [5]

The reflected beam from the sample arm can be described with

$$E_S = \frac{E_i}{\sqrt{2}} [r_S(z_S) \otimes e^{i2kz_S}]. \quad (2.4)$$

Since normally the sample reflectivities are very small, the returned reference field is stronger than the reflected sample field most of the time. Coming back to the example with discrete reflectors, the reflected reference beam can be written as

$$E_R = \frac{E_i}{\sqrt{2}} r_R e^{i2kz_R}, \quad (2.5)$$

while the reflected sample beam can be written as

$$E_S = \frac{E_i}{\sqrt{2}} \sum_{n=1}^N r_{Sn} e^{i2kz_{Sn}}. \quad (2.6)$$

The detector signal (generated photocurrent at the detector) is proportional to the square of the sum of the fields integrated over the response time of the detector (see equation 2.7).

$$I_D(k, \omega) = \frac{\rho}{2} \langle |E_R + E_S|^2 \rangle \quad (2.7)$$

with ρ as the responsivity of the detector (units Amperes/Watt). After expanding the magnitude squared functions from equation (2.7), the dependency upon the temporal angular frequency is eliminated. This leaves the temporally invariant terms

$$\begin{aligned} I_D(k) &= \frac{\rho}{4} [S(k)(R_R + R_{S1} + R_{S2} + \dots)] \\ &+ \frac{\rho}{4} [S(k) \sum_{n=1}^N \sqrt{R_R R_{Sn}} (e^{i2k(z_R - z_{Sn})} e^{-i2k(z_R - z_{Sn})})] \\ &+ \frac{\rho}{4} [S(k) \sum_{n \neq m=1}^N \sqrt{R_{Sn} R_{Sm}} (e^{i2k(z_{Sn} - z_{Sm})} e^{-i2k(z_{Sn} - z_{Sm})})], \end{aligned} \quad (2.8)$$

with $S(k) = \langle |s(k, \omega)|^2 \rangle$ the power spectral dependence of the light source. Since most light source spectra used in OCT systems have approximately a Gaussian-shape, a Gaussian-shaped light source spectrum is used for $S(k)$. Furthermore, it has useful Fourier transform properties. The normalized Gaussian function $S(k)$ and its inverse Fourier transform $\gamma(z)$ can be written in the form of

$$\gamma(z) = e^{-z^2 \Delta k^2} \xleftrightarrow{F} S(k) = \frac{1}{\Delta k \sqrt{\pi}} e^{-[\frac{(k-k_0)}{\Delta k}]^2}, \quad (2.9)$$

with k_0 the central wavenumber of the light source spectrum and Δk its spectral bandwidth. The inverse Fourier transform of the source spectrum $\gamma(z)$ is called ‘coherence function’ and describes the axial point spread function (PSF) in OCT. Its full width at half the maximum (FWHM) value is called coherence length l_c of the light source.

In order to get a relation between the detector signal and the depth dependent structure information, a Fourier transformation has to be applied. With the help of the convention for Fourier transformations (see equation 2.10) and the convolution property of Fourier transformation (see equation 2.11), plus using the Euler’s rule as well as shifting due to the delta function, the Fourier transform is calculated.

$$\cos(kz_0) \leftrightarrow \frac{1}{2} \delta(z - z_0) + \frac{1}{2} \delta(z + z_0) \quad (2.10)$$

$$f(z) \otimes g(z) \leftrightarrow F(k) * G(k) \quad (2.11)$$

This leads to the formula for an ‘A-scan’, which contains the depth informations:

$$\begin{aligned}
i_D(z) = & \frac{\rho}{8} [\gamma(z) [R_R + R_{S1} + R_{S2} + \dots]] \\
& \text{'DCTerms'} \\
& + \frac{\rho}{4} \sum_{n=1}^N \sqrt{R_R R_{S_n}} [\gamma[2(z_R - z_{S_n})] + \gamma[-2(z_R - z_{S_n})]] \\
& \text{'Cross - correlationsTerms'} \\
& + \frac{\rho}{8} \sum_{n \neq m=1}^N \sqrt{R_{S_n} R_{S_m}} [\gamma[2(z_{S_n} - z_{S_m})] + \gamma[-2(z_{S_n} - z_{S_m})]] \\
& \text{'Auto - correlationTerms'}
\end{aligned} \tag{2.12}$$

Equation 2.12 can be split into three parts:

- DC term: It is a constant, non-interferometric intensity term, dependent on the sample and reference power reflectivities and the light source wavenumber spectrum. If the reference reflectivity is far larger than the sample reflectivity, the DC term is the dominant one.
- Cross-correlation term: It represents the interference between the matching sample and the reference beam. Since this term contains the structural information of the sample structure, it is the desired component for OCT imaging.
- Auto-correlation term: It represents the interference, which occurs between the different sample reflectors. In order to decrease autocorrelation artifacts, the reference intensity can be increased.

For a better understanding of equation 2.12, it is illustrated in figure 2.8 with different numbers of sample reflectors. In the case of a single reflector, only the DC term and the cross-correlation term between the sample and the reference beam are present. Its source spectrum is modulated by a simple cosinusoid, which has a period that is proportional to the distance between the sample and the reference beam, while in the case of multiple reflectors, the source spectrum is modulated by multiple cosinusoids. The frequency and amplitude of each cosinusoid depends on the sample reflection and position which gives rise to it. Another difference to the single reflector is the fact that autocorrelation components appear.

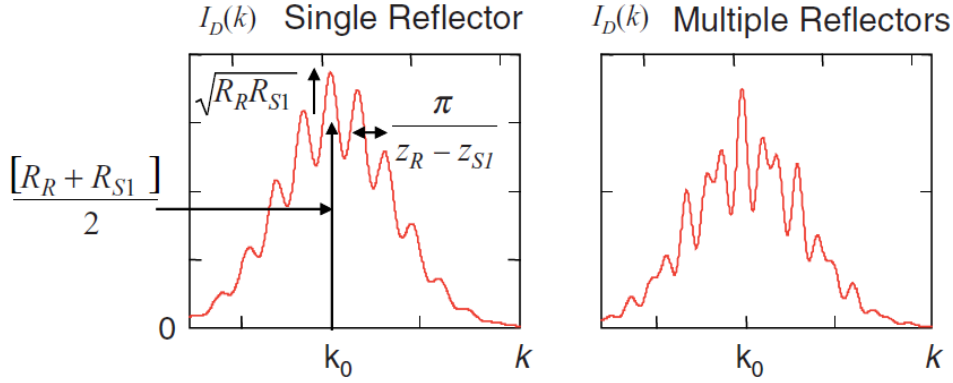


Figure 2.8: The spectral interferogram: For a single sample reflector (left) the cross-correlation component rides on top of the amplitude of the DC term $\frac{[R_R + R_{S1}]}{2}$. In the case of multiple reflectors (right), the cross-correlation component is a superposition of cosinusoids [5].

Equation 2.12 is plotted in figure 2.9 for the example of discrete sample reflectors and a Gaussian-shaped source spectrum.

The complex conjugated term of equation 2.12 can be seen on the left side of figure 2.10. Since it contains the same information as the right side, it gets removed during the image processing process.

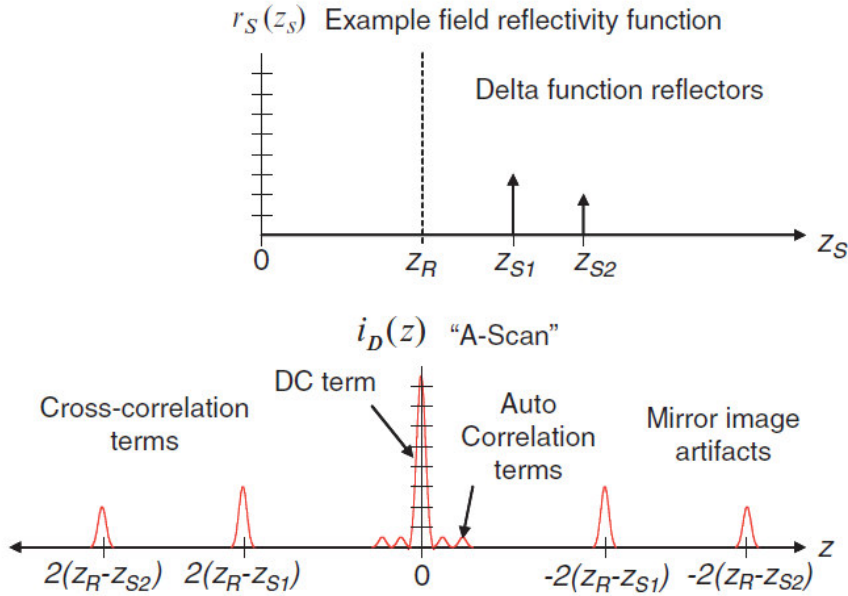


Figure 2.9: An illustration of the example field reflectivity function (top). The resulting A-scan from FD low-coherence interferometry from equation 2.12 (bottom) [5].

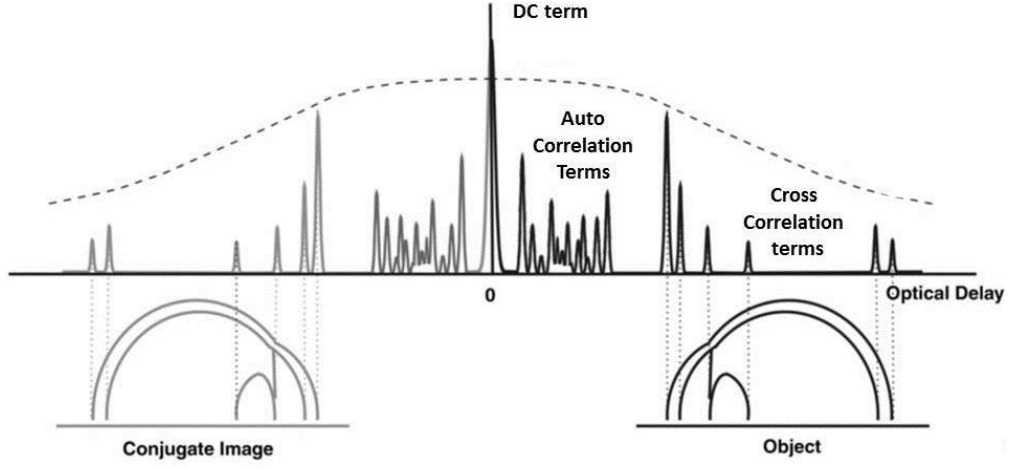


Figure 2.10: The detected signal at the photodetector with the DC-term of the reference beam in the middle, the auto-correlation term from the self-interference of the backscattered light and the cross-correlation term with the structural information [6].

2.1.3 Resolution

Axial resolution [5]

For a Gaussian spectrum, the axial resolution l_c is proportional to the squared center wavelength λ_0 of the light source, as can be seen in equation 2.13. Furthermore, it is inversely proportional to the full width at half maximum (FWHM) $\Delta\lambda$ of the power spectrum.

$$l_c = \frac{2\ln(2)\lambda_0^2}{\pi\Delta\lambda} \quad (2.13)$$

From this equation can be seen that in order to achieve high axial resolution of a SS-OCT system, a broadband light source is required. This behavior is illustrated in figure 2.11.

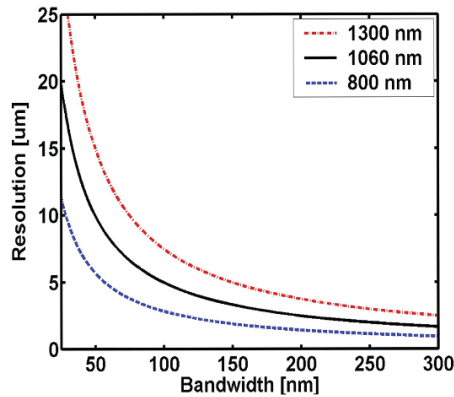


Figure 2.11: Axial resolution vs. bandwidth of light sources for different center wavelengths (800nm, 1000nm, 1300nm)[5]

Lateral resolution [5]

The full width at half maximum power of the PSF of an OCT system is characterized by the lateral resolution $\delta(x)$. Equation 2.14 shows that while the lateral resolution is proportional to the center wavelength λ_0 of the light source, it is inversely proportional to the numerical aperture NA. There is only the need to describe one lateral dimension, since the optical system is cylindrically symmetric.

$$\delta(x) = 0.37 \frac{\lambda_0}{NA} \quad (2.14)$$

2.1.4 Angiography

The basic angiography theory is adapted from [5] and [6].

Angiography is a contrast agent based medical imaging technique that was developed in 1927 by Egas Moniz [1]. He used it for the imaging of cerebral vessels. Nowadays, this imaging technique is used to visualize blood vessels and organs in an organic sample in general. Compared to other angiography methods, OCT angiography can provide vascular contrast in a depth resolving manner with high resolution without the need of contrast agents. This is a great benefit for the patients in research studies, since contrast agents can have many side effects such as nausea, allergic shock or vomiting. With the help of OCT angiography, biomarkers for disease diagnoses of ocular vascularizations like glaucoma, diabetic retinopathy or age-related macular degeneration can be found.

The basic of OCT angiography lies in the speckle and phase difference between two B-scans imaged at the same lateral position. On the one hand, speckle (see figure 2.12) is a source of noise, but on the other hand, it is a carrier of information about tissue microstructure in images of highly scattering biological tissues. Not only are speckles affected by the structure and the motion of the sample, but also by the optics in the sample path and the properties of the light source. It is an interference phenomenon that occurs when interfering coherent light with random phases. Therefore, speckles are the result of superposition of many random wavelets.

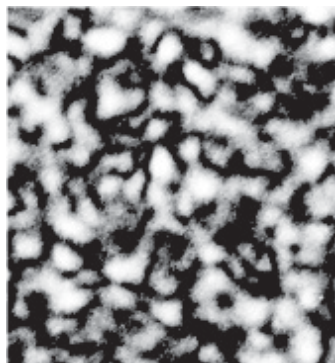


Figure 2.12: *Laser speckle that appears on a white piece of paper that is illuminated by coherent laser radiation (photographic image) [5]*

The measured intensity depends on the detector efficiency and the intensity of

the backscattered sample light. The latter changes over time. This leads to a Rayleigh distribution for the speckle. Since speckle is sensitive to motion, it can be used for vessel detection since they are perfused by moving blood particles. The speckle changes during motion, while it behaves like noise in a static structure. This behavior is used in the so-called speckle variance OCT (SV-OCT). When calculating the intensity variance between two or more tomograms at the same transverse position, microvasculature can be visualized. The contrast in an image is generated by the speckle variance between static structure and blood flow. For calculating the speckle variance, the logarithmic intensity of the tomograms is used, as can be seen in equation 2.15.

$$I(x, y, z) = 20 * \log[|FFT(I(x, y, k))|] \quad (2.15)$$

with k as the wavenumber that after the FFT corresponds to the depth coordinate z and the tomograms $I(x, y, z)$. For SV-OCT, the squared intensity speckle difference between two successive tomograms is calculated (see equation 2.16).

$$D(x, y_i, z) = [I(x, y_{i+1}, z) - I(x, y_i, z)]^2 \quad (2.16)$$

with $i = 1 \dots N$, N as the number of tomograms taken at the same vertical position. For the images used for this thesis, N equals 4, which means that four full B-scans are acquired within $20 \mu s$ at the same position. To get rid of sample movement or scanner position changes, a threshold for high speckle variances is set (see equation 2.17). Otherwise the speckle variance profile of the other B-scans couldn't be observed.

$$M(y) = \sum_{i=0}^{N-1} ([\sum_{x,y} D(x, y_i, z)] < T) \quad (2.17)$$

with N as the number of tomograms taken at the same vertical position. Finally, the vascular contrast $V(x, y, z)$ is calculated by averaging over the thresholded variances M (see equation 2.18) [3].

$$V(x, y, z) = \frac{1}{M(y)} \sum_{i=0}^{N-1} ([\sum_{x,y} D(x, y_i, z)] < T) * D(x, y_i, z) \quad (2.18)$$

2.2 Medical Image Processing

The main goal of this thesis was programming image processing algorithms for images recorded with OCT. Another challenge was to make these algorithms fully automatic, making them suitable for research studies with a great number of patients. Furthermore some already existing code had to be modified to be fully automatic as well. The theoretical aspects of the used image processing techniques are presented in this chapter.

2.2.1 Shortest Path Problem

One task for this thesis was to adapt and improve an algorithm for a retinal layer segmentation in order to get the desired retinal layer boundaries (see chapter 3.3.2). A very useful method for segmentation issues in image processing is using a shortest path algorithm. To deal with the shortest path problem, an image is divided into n nodes. Each of these nodes is connected to all its surrounding nodes through edges, which represent a transition from node to node. In the next step, a weighting factor $w_{i,j}$ is calculated with a cost function that indicates how expensive the transition from node N_i to node N_j is. After setting a start point N_1 , all possible paths to the end point N_n have to be found with the restriction that one can only get from one node to another if they are linked with an edge. The cost C of a path p can be attained by summing up all weights of the edges that have been passed on the way to the end point.

$$C_n = \sum_p w_{i,j} \quad (2.19)$$

After calculating the cost of every possible path, the shortest path, i.e. the path with the lowest cost can be found.

$$\textit{shortest path} = \textit{Min}(C_n) \quad (2.20)$$

The general shortest path problem can be seen in figure 2.13, where arrows are used to indicate the edges between the nodes. The numbers close to each edge indicate the weighting factor. The challenge of this approach is finding a suitable cost function for the present problem (see chapter 3.3.2). Often, a gradient-based cost function is used.

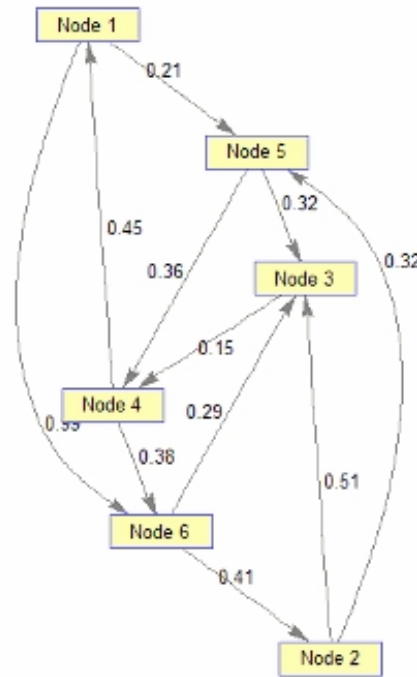


Figure 2.13: Shortest path problem with nodes, edges represented with arrows between the nodes and the corresponding weighting factors as number on the edges [15]

2.2.2 Clustering

The basic clustering theory is adapted from [2].

Another task for this thesis was to develop an algorithm for major vessel segmentation. For this purpose, a clustering method was used. Clustering is an unsupervised learning method to divide data into classes or groups. These classes or groups are the so-called clusters. The difference between unsupervised and supervised learning is that when using unsupervised learning methods, one does not always know the number of clusters and the data does not have a class label. The division of the data $X = (x_1, x_2, \dots, x_N)$ into m Cluster C_1, \dots, C_m is called m -clustering if the following conditions are true:

- $C_i \neq \emptyset, i = 1, \dots, m$
- $\cup_{i=1}^m C_i = X$
- $C_i \cap C_j = \emptyset, i \neq j, i, j = 1, \dots, m$

The vectors x_i from the cluster C_i are more similar to each other than to the vectors in the other clusters. For finding clusters, criteria have to be defined to match them into the according cluster. These criteria depend highly on the data. Popular criteria for clustering are, for example, the distance between two data

points or the scalar product or the Pearson correlations coefficient. A well-known algorithm for clustering is, for example, the k-means algorithm.

2.2.3 Image Registration

The basic image registration theory is adapted from [10].

Movement of the eye during the measurement causes motion artifacts within the B-scans. In order to get rid of these artifacts, an image registration algorithm has been developed. Image registration is a process where two images (2D or 3D) are tried to be matched by gaining correspondences between positions in each image (see figure 2.14 (left)). In order to do so, the target image has to be transformed in such way that the similarity between the target image and the source image is maximized. What kind of similarity measurement is used depends on the present problem. The transformation function can perform a simple translation or rotation, but also non-rigid transformations. If source and target image are pictured with a different modality, a multi-modal registration has to be used, leading to different kinds of similarity measurements (see figure 2.14 (right)). Examples for single-modal similarities are the sums of squared differences, sum of absolute differences, correlation and the normalized cross correlation. For multi-modal image registration, intensity remapping or gradient correlation can be used.

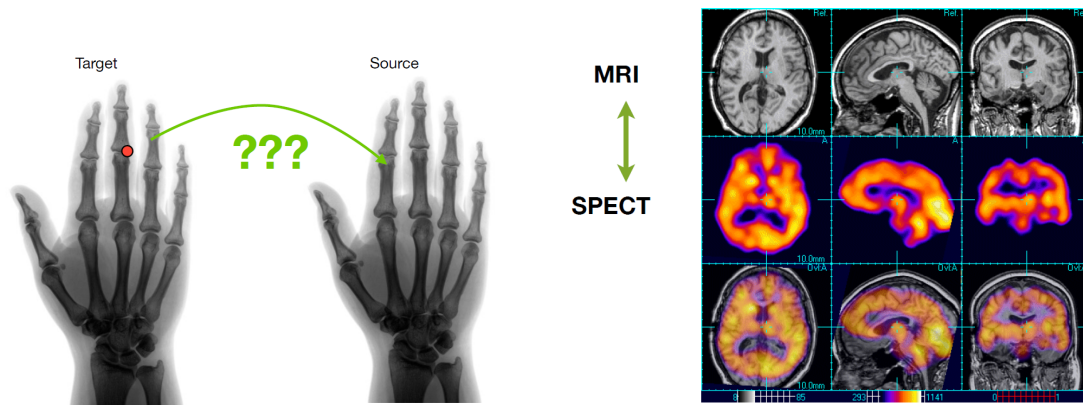


Figure 2.14: Image registration: Source and target image recorded with the same modality (left) and with different modality (right) [10]

2.3 The Human Eye

The basics of this chapter are adapted from [7].

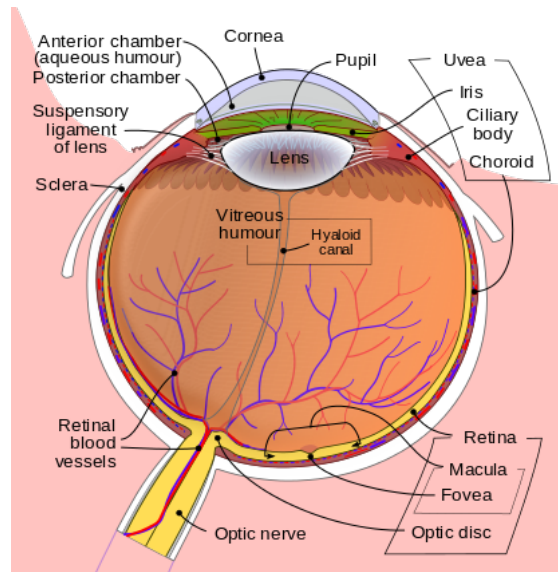


Figure 2.15: Schematic diagram of the human eye [16]

Because of the importance of the eye – as one of the five sensory organs of the human body – in our everyday life, it is mandatory to understand every single detail of it and to therefore keep researching on it. When it comes to the progress of seeing, the retina plays a significant role since it contains the sensory cells and neurons that are responsible for converting and forwarding a light beam to the brain. As can be seen in figure 2.15, the retina is the most inner layer of the eye. After the light has entered the eye through the pupil, it gets refracted onto the retina, where our photoreceptor cells – the cones and rods – are embedded. The retina itself consists of ten layers (see figure 2.16 (from front exterior to back of the head)):

- Inner limiting membrane (Membrana limitans interna, ILM)
- Nerve fiber layer (Stratum neurofibarum, NFL)
- Ganglion cell layer (Stratum ganglionare fasciculi optici, GCL)
- Inner plexiform layer (Stratum plexiforme internum, IPL)
- Inner nuclear layer (Stratum nucleare internum, INL)
- Outer plexiform layer (Stratum plexiforme externum, OPL)
- Outer nuclear layer (Stratum nucleare externum, ONL)
- External limiting membrane (Membrana limitans externa, OLM)
- Layer of rods and cones (Stratum neuroepitheliale retinae)
- Retinal pigment epithelium (Stratum pigmentosum retinae, RPE)

The retina consists of three consecutively connected neurons: photoreceptors, bipolar cells and the ganglion cells. The incoming light beam passes through all the retinal layers until it reaches the photoreceptors (first neuron). The photoreceptor layer in the retina periphery consists of rods and cones. The retina contains about 7 million cones and about 120 million rods. The second neuron consists of bipolar cells, which are part of the INL. After the bipolar cells receive the signal from the photoreceptors, they process it to the ganglion cells. The third neuron is formed by the ganglion cells, whose axons meet at the papilla. From there, they build the optic nerve from which the visual information is transmitted to the brain.

Within the retina there are two characteristic points: the optic nerve head (ONH) and the fovea centralis. The fovea centralis is a small pit in the center of the retina that contains no vessels. The pit is called Foveola and contains only cones. Because of the highest density of photoreceptors in the fovea, it is the point of sharpest vision. The cones are responsible for color vision, as there are three types of cones for red, green and blue. In contrast, the ONH is the point with no vision at all. It is not only the exit point for the ganglion cell axons but also the entry point for the major blood vessels that supply the retina.

The vessels that enter the retina through the ONH are the arteria centralis retinae and the vena centralis retinae. The arteria centralis retinae arises from the arteria ophthalmica and is responsible for the blood supply from the inner retinal layer to the INL (included). It branches out into the NFL. Since the retinal arterioles are auto-regulated, they adjust their vessel diameter and hence the blood perfusion, depending on the demands. The vessel diameter is increased if a CO_2 -accumulation or an O_2 -shortage occurs. The outer retinal layer is provided by the arteriae chorioideae.

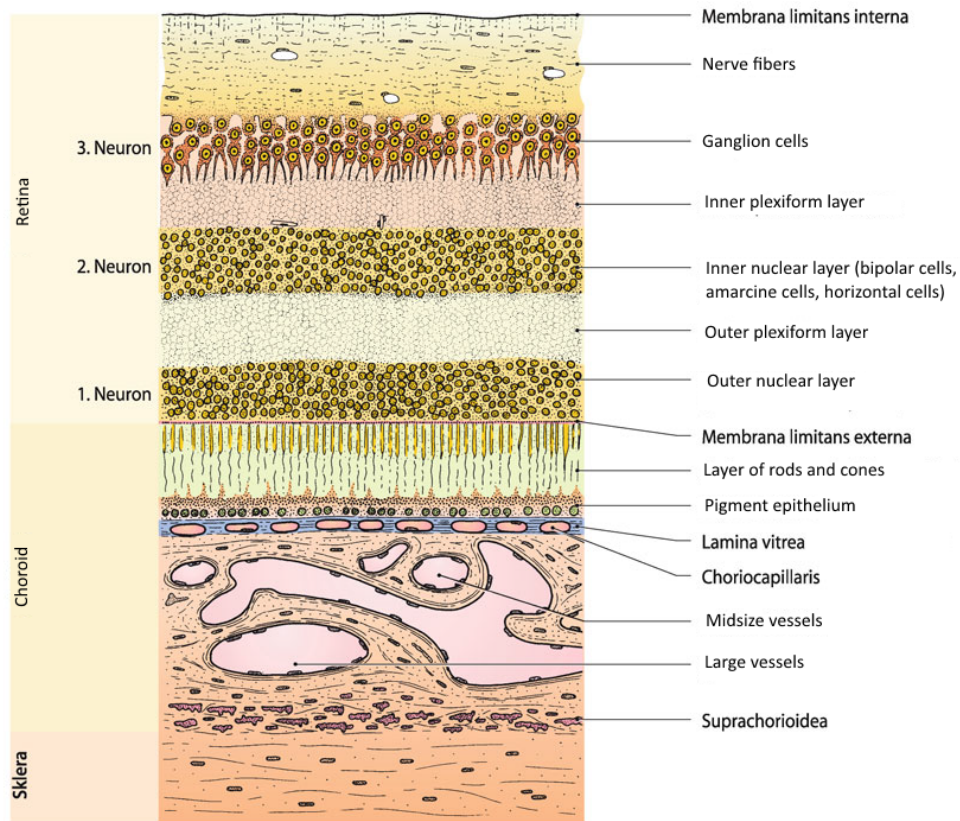


Figure 2.16: Schematic cut through the retina and the choroid [7]

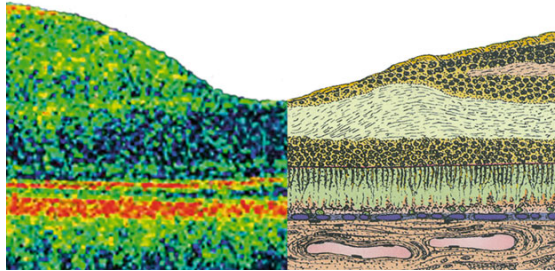


Figure 2.17: A B-scan of the retina recorded with an OCT compared to the histological retinal structure [7]

Glaucoma:

The participating patients of the research studies for which the retinal perfusion parameters were calculated (see chapter 3.3.5) suffer from the eye illness glaucoma. Glaucoma is one of the most frequent reasons for blindness. Because of glaucoma, around 6.7 million people go blind per year all over the world [7]. It is the second most frequent reason for blindness in industrial countries and in developing countries.

The glaucoma is defined as a potentially progressive and characteristic optic neuropathy, that can lead to visual field defects if the harm continues. The intra-ocular

pressure is the modifying key factor in the course of this disease. The diagnosis of the glaucoma is based on morphological aspects such as the vitality of the margin, the visibility of nerve fiber failures, the presence of papilla-margin-perfusion and the functional examinations with the help of computational perimetry. Furthermore, it is based on morphometric medical findings, which currently are mainly gained with the help of SD-OCT. The peripapillary NFL thickness was found to be an important indicator for the diagnosis of glaucoma some years ago. Recent commercial devices have the ability to measure the margin thickness. Clinical studies have shown that the vessels which provide the NFL and their perfusion play an important role in the pathophysiology of the glaucoma. It has been shown, for example, that people with low blood pressure have a higher risk to develop a glaucoma than people with a normal blood pressure [12]. With OCT, it is possible to gain 3D vessel architecture within the NFL.

For an ongoing research study, data was provided to examine whether there is a correlation between the vessel density and the NFL thickness in the cross section. Patients with a notch-sign (localized nerve fiber breakdown on the edge of the papilla) are imaged with the help of SD-OCT and OCT-A. The determination of the NFL thickness to vessel density proportion could also give information on whether the damaging of the vessels appears before the damaging of the NFL or if this correlation is vice versa. This question is currently not clarified and is essential, but missing information about the pathophysiology of the glaucoma. Therefore, the NFL-thickness was calculated with the help of the retinal layer segmentation (see chapter 3.3.2). Furthermore, microvascular perfusion parameters were defined and calculated (see chapter 3.3.5).

3 Methodology

The images of the retina used for developing and testing the segmentation algorithms in this thesis were imaged with a SS-OCT by Laurin Ginner. The imaged persons are participants of various medical research studies. The data processing has been performed retrospectively and only anonymized patient data was accessible. Depending on the research study, only one or both eyes were imaged. Furthermore, some patients were imaged with two different Field of View (FOV) settings. Before the retinal perfusion parameters can be calculated, several image processing steps have to be made.

In this chapter, these necessary steps are explained in detail. Furthermore, it covers how the theoretical aspects described in chapter 2 are applied on the SS-OCT data. Before the image processing methods are described, the general workflow and the used SS-OCT are described in detail. At the end of this chapter, the perfusion parameters are introduced.

3.1 Workflow

To obtain the microvascular parameters for the research studies, several steps have to be made after the imaging of a patient. The general workflow from the imaging of the patient to the microvascular parameters is described below.

The raw anonymized OCT data have been used in the post-processing. On the OCT files, the k-mapping and the Fourier Transform are applied with the help of a LabView algorithm, whereby the measured 1600 B-scans (four images at 400 lateral positions) are gained with a resolution of 1600x400 pixels. After that, these 1600 B-scans are combined into a tomogram from which the speckle variance angiography is calculated with the help of a Matlab algorithm, resulting in a 1600x400x400 matrix. For this purpose, the four images recorded at the same lateral position are merged into one image by calculating the mean value of them. In the next step, the projection of the angiography is calculated with Matlab, so that the quality of each measurement can be rated more easily. For the evaluation of the image quality, each angiography projection has to be analyzed in detail. Afterwards, the images with the highest axial resolution are gained from the measurement with the best quality only, since processing all measurements from a patient would be very time-consuming and would take a lot of disc space. On these images, the shortest path algorithm coded in Matlab is applied in order to get the retinal layer segmentation. The retinal layers can be converted so that they fit the corresponding angiography. With the help of the retinal layer segmentation, the noise above the retina and the layers that are not desired for the research study can be removed from the angiography. After the maximum projection of the segmented angiography has been calculated, the vessel segmentation algorithm coded in Matlab can be applied. The last applied algorithm coded in Matlab removes the segmented vessels, divides

the maximum projection or 3D stack into clusters and calculates the microvascular parameters of the desired retinal layers within each cluster.

3.2 OCT

3.2.1 OCT System Setup

The images used for the medical image processing are recorded with the SS-OCT setup as described in the thesis by Laurin Ginner [6]. In figure 3.1, the optical setup of the used OCT can be seen.

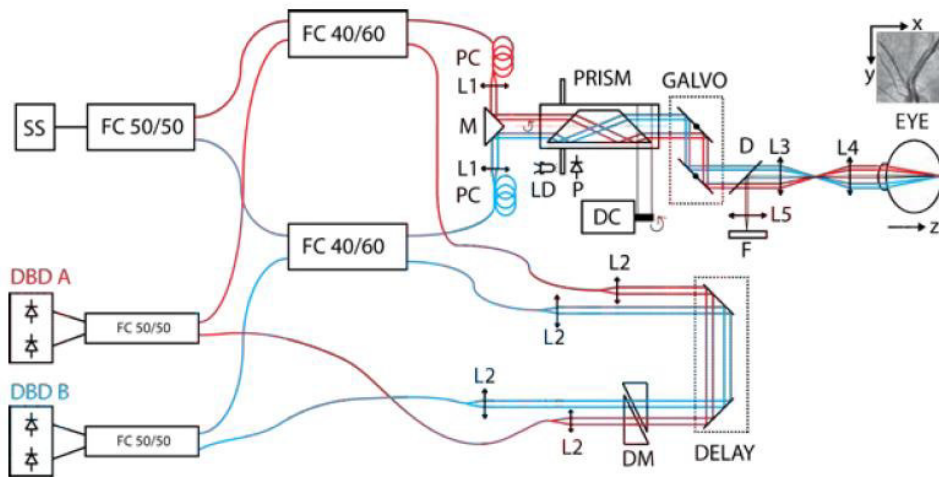


Figure 3.1: Schematic of the OCT setup. The red and blue lines show the path-way of the two beams [6]

It is a dual beam Doppler OCT system with a swept source, which operates at a center wavelength of 1050nm. The used swept source is a multiplex source by Axsun (A1300467) with an A-scan frequency of 200kHz and a bandwidth of 105.62nm. Thus, the axial resolution is around $5\mu\text{m}$ in air. A fiber couple (FC) with a coupling ratio of 50:50 splits the light from the swept source into two beams. Each of this beam is split again by a fiber coupler with a coupling ratio of 40:60, leaving 40% of the intensity for the sample arm and 60% for the reference arm. Afterwards, the sample beam passes through a Dove prism so that the beam can be rotated by 360° , followed by a galvo scanner, which is able to scan over a maximum of 16° field of view (FOV) horizontally and vertically. Next, the sample beam travels to the eye. The reflected beam from the eye and the reference beam interfere and are detected with a detector by Exalos (EBR37000x-01), which is a dual-balanced detector. To match the coherence window with the sample arm, the reference arm is axially movable. To get rid of the dispersion of the reference beam, it travels through a dispersion compensating glass prism. A telescope (L3 and L4) with an angular magnification of 1.5 times is placed in the sample arm, which enables a spot size on the retina of $25\mu\text{m}$, from a beam with a size of about 1.3mm at the cornea. Each beam has a total power of about 1.2mW at the cornea,

giving a sensitivity of about 94dB. This is consistent with the ANSI standards safe exposure limits. For digitalizing the signal, a 12bit analog-to-digital converter ATS9350 from Alazartech with a sample rate of 250MSamples/s is used. The 12 Bit binary spectral information is stored in OCT files. These files also include a header with the information on the scanning angle, remapping and other notations.

3.2.2 Swept Source OCT

For a SS-OCT system, a fast tunable laser source is needed. Therefore, a SS-OCT system with an integrated swept source from Axsun(A1300467) is used. It is a multiplex swept source that consists of two interleaved lasers, each operating at 100kHz. They can sweep alternately so that after the sweep of the first laser is done, the forward sweep of the other laser continues, while the backsweep of the first laser gets suppressed. With this method, a duty cycle of nearly 100% is reached, allowing the frequency of 100kHz to be doubled to 200kHz. This behavior is illustrated in figure 3.2: The left curve shows the timing of the single source, where the backsweep is suppressed after the first sweep. The right curve shows the two interleaved sources, where the second source jumps in while the backsweep of the first source is suppressed.

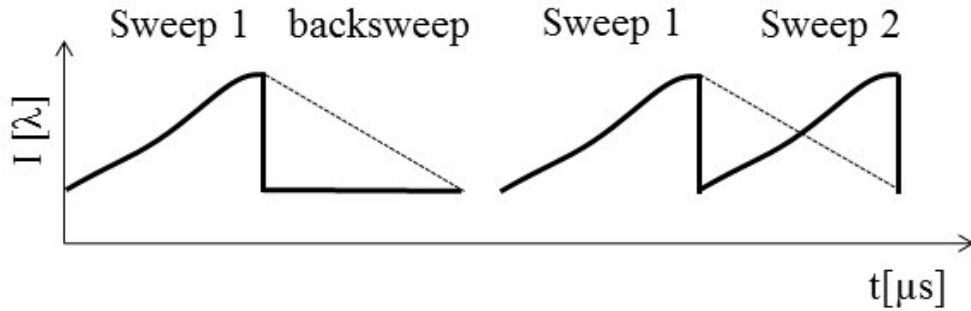


Figure 3.2: The sweep structure of the used Axsun laser [6]

In order to get the depth-profile, a Fast Fourier Transformation (FFT) needs to be applied, leading to two images from each sweep. These can be interleaved in post-processing. Due to the increase of the A-scan rate from 100kHz to 200kHz, the lateral sampling can be doubled, leading to improved imaging performance. The swept source has a central wavelength near the infrared at 1050nm and a sweeping broad bandwidth of 105.62nm, leading to an axial resolution of 5 μ m in air.

With a method based on splitting the optical spectrum, the SS-OCT system further increases the acquisition speed and spatial sampling without increasing the measurement time. For this split-spectrum approach, the recorded spectra are split into two sub-spectra, each with half the optical frequency (see figure 3.3). The spectra are recorded over time by using continuous laser scanning in fast axis direction. The scanner records at a lateral position with the first half of the spectrum. During the recording with the other half of the spectrum, the scanner is

already located at another lateral position.

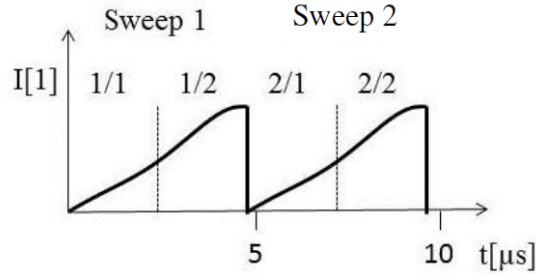


Figure 3.3: *Split spectra approach [6]*

This allows to double the FOV from 8° with the 100kHz acquisition to 16° with the 400kHz acquisition. Due to the spectral splitting, the bandwidth of each sub-spectrum is 52.81nm, while preserving the same sampling density. This decreases the axial resolution to $10\mu\text{m}$ (see equation (2.13)).

The 100kHz acquisition (one sweep) has 400 lateral sampling points, while the 200kHz acquisition (two sweeps) has 800 sampling points and the 400kHz acquisition (split-spectra) has 1600 sampling points. The acquisition time is 7.8 seconds. Thus, the split spectra approach increases the number of lateral sampling by a factor of four, allowing it to increase the FOV to 16° without any resolution and contrast losses. The image intensity is saved as an unsigned 16bit TIF file. Furthermore, the angiography can be calculated by applying the speckle variance method described in chapter 2.1.4. The difference in results from the three explained methods can be seen in figure 3.4 on an OCT angiography maximum intensity projection.

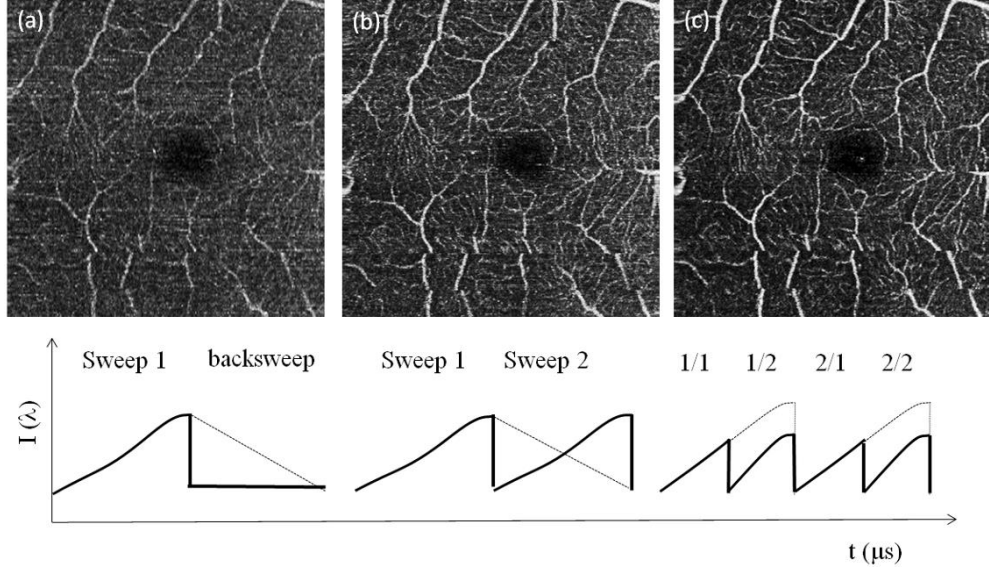


Figure 3.4: Images recorded around the Fovea with different sweep structures: (a) Standard 100 kHz SS-OCT with 8° FOV, (b) 400kHz acquisition with 16° FOV and (c) the 8° FOV section of the 16° FOV image. The latter shows the same vessel structure with a better SNR [6]

3.2.3 Remapping

The basic remapping theory is adapted from [6] and [5]. To obtain the depth profile (A-scan) in FD-OCT, a Fourier transformation has to be applied to the optical spectrum of the interference at the output of a Michelson interferometer. In the A-scan, the structural information can be observed. With the help of the Fourier transformation, the physical distance z can be related with the wave number ($k = 2\pi/\lambda$). After Fourier-transforming, a depth-dependent broadening of the coherence peak can be observed, which destroys the exact depth position. This broadening occurs due to the fact that the spectra obtained with FD-OCT does not necessarily have to be evenly spaced in k -space. Therefore, the data has to be preprocessed before the FFT can be applied in such a way that it is evenly spaced in k -space, which is called remapping. For this purpose, the wavelength requires an accurate assessment to each corresponding spectral element so that the depth coordinate relates to a specific wavelength. Based on the research of A. F. Fercher and R. Leitgeb, Wojtkowski et al. were the first to notice the importance of proper wavelength assignment for SD-OCT [17]. One method for remapping is to perform a separate measurement of a reflective surface at different positions in the sample arm while another method is to impose a known modulation onto the spectrum, which can be used for calibration. Another possibility is using a hardware- k -triggering.

In the SS-OCT that imaged the used images, the reference interference pattern is measured with a single reflector in the sample arm. The Hilbert transformation is applied to this interference pattern, which allows getting its phase signal. Af-

terwards, a spectral interval can be selected with an almost linear phase change. This interval is used in order to get a spectrum that is evenly spaced in k-space. This way, the axial resolution can be regained.

Since the used SS-OCT system uses different lasers for each sweep, the remapping has to be calculated separately for each sweep. Furthermore, each sweep is split into two halves which also need to be remapped separately. Hence a Hilbert transformation is applied to all four spectra and an almost linear phase change section is selected. This way, each sweep can be remapped separately.

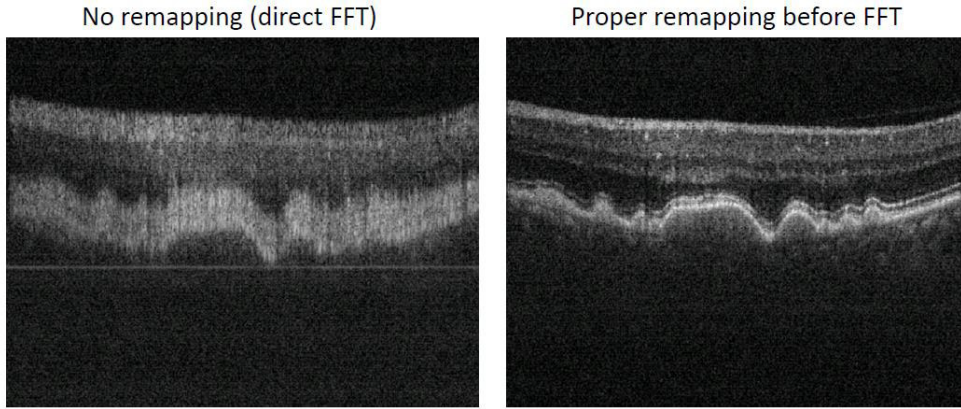


Figure 3.5: *No remapping vs proper remapping: Without remapping, a broadening of the depth structure appears, which makes it impossible to get the exact depth position [6]*

3.3 Image Processing

This chapter describes how the theory of each image processing step (see chapter 2.2) is applied to the images recorded with the SS-OCT. Furthermore, some steps of the programmed algorithm are explained in detail. For a better understanding of the following chapter, the pixel indication used in Matlab is shown in figure 3.6. Matlab uses a pixel coordinate system in which the images are treated as a grid of discrete elements. It is arranged from top to bottom and from left to right. The coordinate of a pixel uses the notation (row,column). In a 3D array (see figure 3.7), a pixel has the coordinate (row,column,page).

	column →			
row ↓	{1,1}	{1,2}	{1,3}	{1,4}
	{2,1}	{2,2}	{2,3}	{2,4}
	{3,1}	{3,2}	{3,3}	{3,4}
	{4,1}	{4,2}	{4,3}	{4,4}

Figure 3.6: *Matlab pixel coordinates notation [15]*

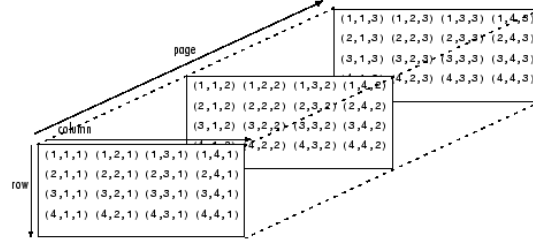


Figure 3.7: *Matlab Multidimensional Arrays: To access e.g. the element in the second row, third column of page 2, the subscription (2,3,2) is used [15]*

3.3.1 Image Registration

A disadvantage of in vivo measurements are motion artifacts in axial and lateral directions obtained by movements of the patients. For a correct calculation of the variance for the angiography (see equation 2.16), the motion artifacts have to be removed. Also when calculating the microvasculature parameters (see chapter 3.3.5), the results would not be accurate if the lateral displacement was not back-shifted. In order to deal with these motion artifacts, a subpixel image registration algorithm by Manuel Guizar-Sicairos et al. is used [8]. The algorithm obtains an initial estimate of the crosscorrelation peak by an FFT (fast Fourier Transform). Afterwards, it refines the shift estimation by upsampling the DFT (discrete Fourier transform) only in a small neighborhood of that estimate by means of a matrix-multiply DFT. The algorithm is used on the angiography B-scans before the variance is calculated. They have a lateral resolution of 1600px and an axial resolution of 400px. Since 1600 B-scans are recorded, a 1600x400x1600 px matrix is gained. The image registration algorithm is used on the data two times, once for the lateral displacement and once for the axial displacement. The result are one lateral and one axial displacement vector. The 200th B-scan has been chosen as a reference image for the lateral displacement. The lateral displacement vector indicates how much each B-scan has to be shifted laterally in relation to the reference image. A pixel with the coordinate (m,n,o) gets the new coordinate (m,n - lateralShift,o) for a negative shift, while it gets the new coordinate (m,n + lateralShift,o) for a positive shift. Therefore, a negative shift implies a shift to the left, while a positive shift implies a shift to the right. After the lateral shift, the B-scan size increases to (1600 + |minimum negative shift| + maximum positive shift)x400x1600px. Instead of a specific reference image, the algorithm for the axial displacement always uses the prior B-scan as reference image. Hence, the axial shift for a pixel is the difference axialShift = $m_2 - m_1$, with (m_2, n_2, o) as the coordinate for the registered pixel and ($m_1, n_1, o-1$) as the coordinate of the correlated pixel from the prior B-scan. The new coordinate of a pixel after registration for a positive shift is (m + axialShift,n,o), while the new coordinate is (m - axialShift,n,o) for a negative shift. This means that a positive shift is a shift downwards in relation to the prior B-scan, while a negative shift is a shift upwards in relation to the prior B-scan.

3.3.2 Retinal Layer Detection

One aim of this thesis was to find the retinal layer boundaries shown in figure 3.8.

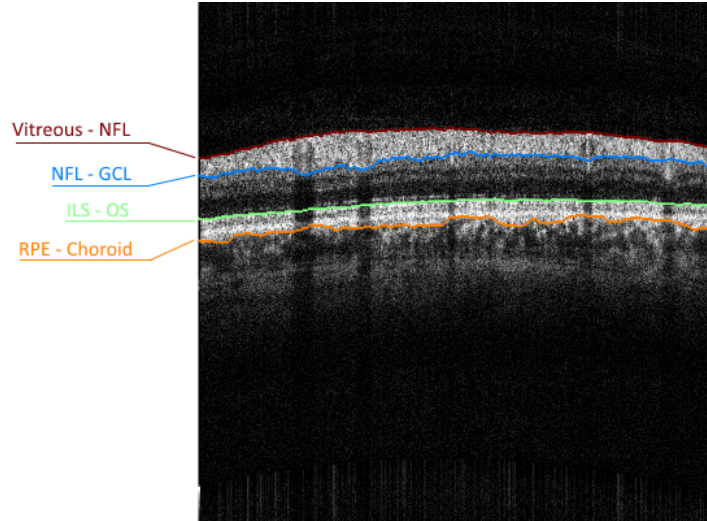


Figure 3.8: Segmentation Layers: Vitreous - Nerve Fiber Layer, Nerve Fiber Layer - Ganglion Cell Layer, Inner Boundary of Inner Segment - Outer Segment, Retinal pigment epithelium - Choroid

Since the eye is spherical, the retina of the human eye is curved as well. Before the retinal layer segmentation algorithm is applied to the images, a flattening algorithm is used on the tomograms. This makes the retinal layer segmentation easier. Furthermore, it is helpful to get an en-face cut of a single layer of the retina from a tomogram. For the flattening the curvature is converted to a static depth position. In order to do this, the maximum intensity position of the RPE over one B-scan has to be detected and afterwards, a low order polynomial fitting of this position is done. With the help of the local difference between the polynomial fitting curve and the constant depth position, each A-scan of a B-scan can be shifted properly [6].

For the retinal layer detection, a shortest path algorithm is used, which is based on the paper by Pratul P. Srinivasan et al. [14]. The algorithm was implemented with Matlab. The algorithm is applied on the B-scans measured with the 100kHz acquisition, since they have a better axial resolution, as has been described in chapter 2.1.3. One measurement of an eye contains 1600 B-scans, where four B-scans are recorded on the same position for more reliable results. Thus, after calculating the mean of these four B-scans, a total of 400 B-scans remain. Since each B-scan of the 100kHz data consists of 400x400 pixels, a 400x400x400 matrix for applying the shortest path algorithm is obtained. One pixel corresponds to an uint16 (16-bit unsigned integer) value depending on its gray scale value, where 2^{16} is a perfect white pixel and 0 a perfect black pixel. For applying the algorithm, nodes and edges have to be applied (see chapter 2.2.1). One pixel corresponds to one node. Since the segmentation code was programmed with the farthest left pixel (m,0)

3. Methodology

as the starting point, each pixel only gets edges to pixels above (m-1,n), below (m+1,n), right above (m-1,n+1), right below (m+1,n+1) or right (m,n+1) to it. Building edges to pixels left (m,n-1), left above (m-1,n-1), left below (m+1,n-1) of it would not be consistent with the biological form of a retinal layer.

As has been described in section 2.2.1, an important step for solving the shortest path problem is to calculate weighting factor $w_{i,j}$ for each edge with a function that fits the problem in question. In the segmentation code, the same function for calculating the weighting factor as in the paper by Srinivasan et al. [14] (see equation 3.1) has been used.

$$w_{i,j} = (2 - (g_i + g_j)) + \lambda_s(|I_i - I_j|) + w_v + w_{min}, \quad (3.1)$$

where:

$w_{i,j}$ is the weight of the edge connecting nodes i and j,

g_k is the normalized vertical gradient of the image at node $k \in i,j$,

λ_s is the ‘similarity factor’ weight,

I_k is the normalized intensity of node $k \in i,j$,

w_v is the ‘vertical penalty’ term to add extra weight to edges going up, down, or diagonally,

w_{min} is the minimum weight term ($1 \cdot 10^{-5}$) added for numerical stability

Due to the gradient term $(2 - (g_i + g_j))$, pixels with large vertical gradients are preferred as a boundary between two retinal layers. To prefer boundaries with similar or hardly changing intensity pixels, the similarity term $\lambda_s(|I_i - I_j|)$ is added. They are normalized linearly so that the pixel values lie between zero and one. At last, a vertical penalty term w_v is added in order to prevent the segmentation from jumping between boundaries.

A path has to traverse edges from the leftmost column to the rightmost column of the image. After calculating the weighting factors for all paths, the shortest path is found according to equation 2.20 in section 2.2.1. This leads to the first retinal layer boundary (Vitreous - NFL). Once the first boundary is segmented, it is used to limit the search space for the missing layer boundaries. Now the shortest path algorithm is applied again to find the next boundary. This process is repeated until all desired layers have been found.

The informations gained by the layer segmentation are used for the ONH segmentation to create a mask of the ONH (see chapter 3.3.3). After finding the ONH mask, a second run of the retinal layer segmentation algorithm is applied. However, this time the algorithm isn’t applied to the ONH area, resulting in a more accurate layer segmentation. The segmentation algorithm returns a 400x400 array for each boundary. The element in the cell (i,j) of an array contains the position measured from the top of the boundary for the j-th A-scan in the i-th B-scan. If

the cell (1,2) of the vitreous - NFL boundary array contains e.g. the number 150, it means that the position of the boundary in the second A-scan of the first B-scan is at the 150th pixel measured from the top.

As has been described in chapter 2.3, the determination of the NFL-thickness can play an important role for patients with Glaucoma. The NFL-thickness along the whole tomogram can be calculated by building the difference between the vitreous - NFL boundary and the NFL - GCL.

3.3.3 Optic Nerve Head Segmentation

Not only does the retinal layer segmentation algorithm have its weakness in the area around the optic nerve head (ONH), but also do later perfusion parameter calculations require the exclusion of the ONH. The algorithm of the ONH segmentation is applied after the first retinal layer segmentation run. The shortest path algorithm returns a rather linear transition over the ONH area of the vitreous - NFL boundary. This behavior is used for the ONH segmentation. The algorithm looks at every pixel $(z+1,j)$ over the whole B-scan, with z as the depth position of the vitreous - NFL boundary and $j = 1,2,...,400$ (lateral B-scan size), i.e. the pixel under the boundary. If this pixel has an intensity beneath a certain threshold, it is assumed that there is no retinal structure but the ONH area. The threshold is used to get rid of noise which is under the vitreous - NFL boundary, although there are still some outliers. To get rid of these outliers, a clustering algorithm (see chapter 2.2.2) is applied to find the biggest cluster (see also chapter 3.3.4), which is assumed to be the ONH. After applying some morphological functions, the algorithm takes all gathered pixels, calculates its centroid and shapes a circle with an area equal to all gathered pixels and the centroid as its center. This circle is assumed to be the ONH mask. This leads to a 400x400px mask.

As a second approach, a semi-automatic method has been programmed. For self-chosen images, the en face image is shown and one can drag a circle around the ONH, creating a mask for its exclusion. This approach was used for images with bad quality.

3.3.4 Major Vessel Segmentation

The segmentation of the major vessels is required due to their high intensity and the shadow they produce, which disturb the perfusion parameter calculations. The major vessel segmentation algorithm uses the en face maximum projection image of the retinal angiography. It is resized into a 800x800px image, where each pixel has a value between 0 and 2^{16} , representing the intensity. In the first step, an intensity threshold T is applied to the image, as the vessels have a higher intensity on the angiography than the microvascular structures do. To determine the threshold, the mean value of the intensities is calculated. Next, a cluster method as has been described in chapter 2.2.2 is applied. To initialize this cluster method, the first non-zero value pixel from the top left corner is put into the cluster C_1 . A pixel (i_1,j_1) with the intensity I fits into the cluster C_n if the following criteria apply to any pixel (i,j) that is already in C_n :

- $|i - i_1| = 1 \vee |i - i_1| = 0 \wedge |j - j_1| = 1 \vee |j - j_1| = 0$
- $I > T$

After all the pixels belonging to the first cluster have been found, this process is repeated until all pixels are sorted into n clusters C_n . Afterwards, the group size of each cluster, i.e. the number of pixels in each cluster, is calculated. Clusters below a certain group size are cut out. Thereby, outliers are removed. In order to find a satisfying intensity threshold and group size threshold, various multiples of the mean value are combined with various group sizes. The results of the different combinations are saved for each patient. By doing so, the best combination of intensity and group size threshold can be found.

3.3.5 Microvasculature Perfusion Parameters

To examine the question whether there is a correlation between the density of microvascular structure and the NFL-thickness, measurement parameters for the microvasculature have to be defined. The parameters from the paper of Chieh-Li Chen et al. have been used [4]. Chen et al. defined three parameters for calculating the perfusion in the optic nerve head, namely flux, vessel area density and normalized flux. In this thesis, the same parameters have been used but applied to the area around the optic nerve head and the fovea. Furthermore, the formulas have been expanded from two dimensions into three dimensions, making comparisons between the 3D data and their maximum projection possible. For the research studies, other parameters such as O_2 -saturation have been measured in a specific area by the doctors running the research study. The goal was to calculate the perfusion parameters in the same area in order to make the results comparable.

For a 2D image the perfusion parameters are defined as follows:

$$Flux = \frac{\sum_{(x,y) \in Area} \frac{I_{Flow}(x,y)}{2^{16}}}{Area} \quad (3.2)$$

$I_{Flow}(x,y)$ is defined as the maximum projection along each A-scan of the angiography intensity values. To normalize $I_{Flow}(x,y)$, it is divided by 2^{16} since the loaded image data are uint16 (unsigned integer with 16 bits), giving the values a range between 0 and 2^{16} . Depending on the research study, these parameters are calculated for a different chosen area. For one research study, the area corresponds to a circle with a chosen radius that fits the measured NFL-thickness area, while for another research study, the radius is chosen that fits the measured O_2 -saturation area. The center of this circle is in the center of the calculated ONH mask or in the center of the fovea. Furthermore, the ONH itself or the center of the fovea is excluded from the area.

The vessel area density is the ratio of the area with vessels to the total area. To differentiate the vessels from noise, only flow signal intensities over a certain

threshold value were taken into account. The threshold was selected by calculating the first minimum of the histogram from the angiographic signal intensities.

$$Vessel\ Area\ Density = \frac{\sum_{(x,y) \in Area} v(x,y)_{Area}}{Area}, \quad (3.3)$$

$$v(x,y)_{Area} = \begin{cases} 1, & \text{if } (x,y) \text{ is a vessel} \\ 0, & \text{otherwise} \end{cases}$$

To calculate the flux within the vessels only, the $I_{Flow}(x,y,z)$ is multiplied with 1 or 0, depending on whether it is found to be a vessel or not (Eq. (3.4)). Thus, it only takes $I_{Flow}(x,y)$ values into account that are defined as a vessel.

$$Normalized\ Flux = \frac{\sum_{(x,y) \in Area} \frac{I_{Flow}(x,y) \times v(x,y)_{Area}}{2^{16}}}{\sum_{(x,y) \in Area} v(x,y)}, \quad (3.4)$$

$$v(x,y)_{Area} = \begin{cases} 1, & \text{if } (x,y) \text{ is a vessel} \\ 0, & \text{otherwise} \end{cases}$$

For calculating the perfusion parameters on 3D data, mainly the area is changed into a volume. The parameters are defined as follows. When evaluating the 3D angiography data, $I_{Flow}(x,y,z)$ is defined as the angiography intensity values. The volume flux (Eq. (3.5)) is defined as the mean flow signal intensity over a volume within a certain radius (size as mentioned above).

$$Volume\ Flux = \frac{\sum_{(x,y,z) \in Volume} \frac{I_{Flow}(x,y,z)}{2^{16}}}{Volume} \quad (3.5)$$

The percentage of vessels within the chosen volume is calculated using the vessel volume density ((3.6)).

$$Vessel\ Volume\ Density = \frac{\sum_{(x,y,z) \in Volume} v(x,y,z)_{Volume}}{Volume}, \quad (3.6)$$

$$v(x,y,z)_{Volume} = \begin{cases} 1, & \text{if } (x,y,z) \text{ is a vessel} \\ 0, & \text{otherwise} \end{cases}$$

The normalized volume flux in equation 3.7 is defined as the flux within the vessels

3. Methodology

over the whole volume.

$$Normalized\ Volume\ Flux = \frac{\sum_{(x,y,z) \in Volume} \frac{I_{Flow}(x,y,z) \times v(x,y,z)_{Volume}}{2^{16}}}{\sum_{(x,y,z) \in Volume} v(x,y,z)}, \quad (3.7)$$

$$v(x,y,z)_{Volume} = \begin{cases} 1, & \text{if } (x,y,z) \text{ is a vessel} \\ 0, & \text{otherwise} \end{cases}$$

As requested by the doctor running the research study, the 2D and/or 3D values were calculated. Furthermore, these parameters were not calculated over the whole image but instead, the image itself was subdivided into a certain amount of clusters as requested by the doctors of the research studies. For each of these clusters, the parameters were calculated separately.

4 Results and Discussion

This chapter contains the results of the data acquired with the help of the algorithms that are described in chapter 3. Not all research studies for which the algorithms were developed have been finished yet. Therefore, this chapter contains information on how well the algorithms have worked on the data, plus a few given examples. The sole research study that has already been published (effective September 2018) is about regional patterns of retinal oxygen saturation by Julia Hafner et al. [9].

4.1 Image Registration

As has been described in chapter 3.3.1, the image registration was applied to the images gained with the 400kHz acquisition before calculating the speckle variance in order to compensate movement artifacts. In figure 4.1 a), a maximum projection of the retina around the ONH with lateral motion artifacts can be seen while in figure 4.1 b), the same image can be seen after all B-scans have been shifted according to the lateral displacement vector, which was calculated with the image registration algorithm.



Figure 4.1: *En face maximum projection of the angiography gained with the 400kHz acquisition before (left) and after (right) shifting the B-scans with the lateral and axial displacement vectors.*

This example illustrates how important the image registration is in order to get a clear view of the vessel structure. With the help of the algorithm, the affected regions were shifted laterally and axially. In figure 4.2, the lateral (a) and axial (b)

4. Results and Discussion

displacement vector of the image in figure 4.1 can be seen. The different pattern of these vectors results in the differently used reference image. While the lateral displacement is calculated regarding one specific B-scan, the axial displacement always uses the prior B-scan. All in all, the algorithm worked very well on the used data.

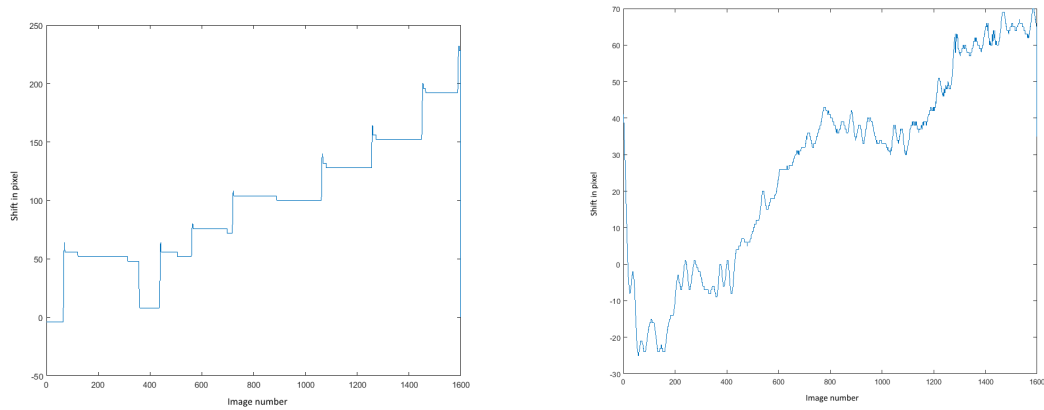


Figure 4.2: *Lateral (left) and axial (right) displacement vector from the shown example in figure 4.1.*

4.2 ONH Segmentation

After applying the ONH segmentation algorithm on the maximum projection of the angiography as described in chapter 3.3.3, a 400x400px mask has been gained. While a pixel with the value 1 (white) indicates that it is a part of the ONH, a pixel with the value 0 (black) is not. This mask can be used to get rid of the ONH, as figure 4.3 shows. Furthermore, a comparison between the original ONH mask and the reshaped ONH mask after the morphological functions have been applied can be seen in figure 4.4.

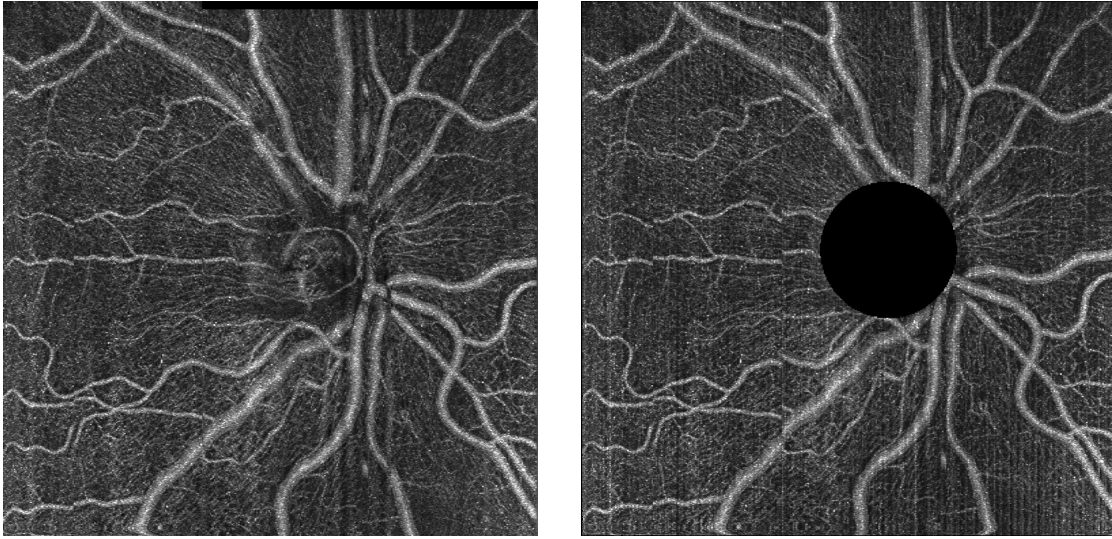


Figure 4.3: *En face maximum projection of the angiography gained with the 400kHz acquisition without (left) and with (right) ONH segmentation.*



Figure 4.4: *An example of an ONH mask calculated with the ONH segmentation algorithm (left) and the same ONH mask after the application of the morphological functions (right).*

4.3 Retinal Layer Segmentation

For the purpose of retinal layer detection, the algorithm described in chapter 3.3.2 was used on the B-scan images recorded with the 100kHz acquisition. The quality of the results of the retinal layer segmentation depends highly on the quality of the images. Taking a look on the equation 3.1 in chapter 3.3.2 for calculating the weighting factor for the shortest path algorithm, the vertical penalty w_v can

be chosen freely. To find the best value of w_v for the faced problem, the layer segmentation was tested on some data set. The algorithm was applied with various w_v values to each test data set. Afterwards, the test results were inspected to find the most fitting value. It was found that the retinal layer segmentation was the most accurate with a value of $w_v = 0.25$.

Depending on the aim of the study, different layer segmentations were required. For the research study of Julia Hafner et al. [9], the layers beginning with the NFL to the RPE are needed. An example of the layer segmentation on a B-scan measured around the fovea with the 100kHz acquisition used for this research study can be seen in figure 4.5.

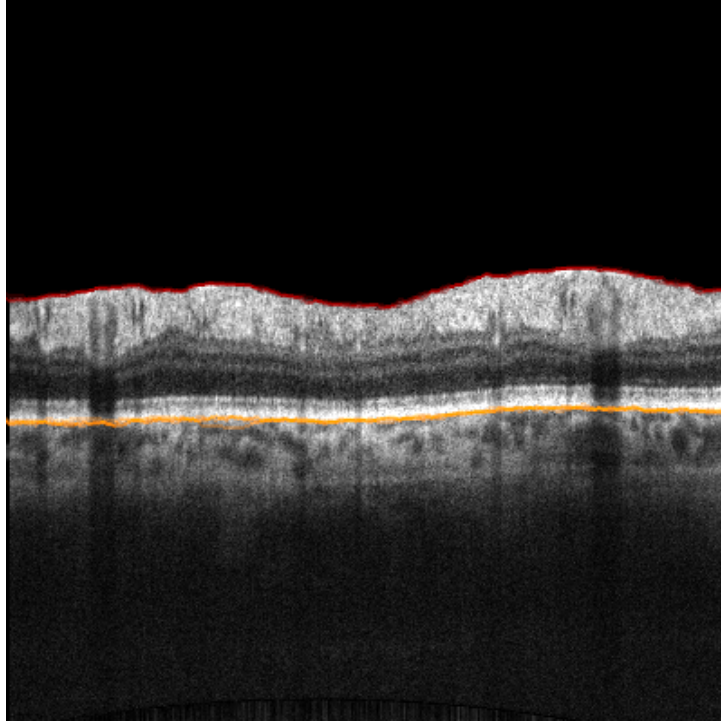


Figure 4.5: Retinal layer segmentation on B-scan acquired with the 100kHz acquisition. The red line shows the vitreous - NFL boundary, while the orange line shows the RPE - choroid boundary as detected by the segmentation algorithm.

The red line indicating the Vitreous-NFL boundary can be detected very accurately, since the gradient of the measured intensities is very high in this area. In some cases, the image quality decreases on the edges of the B-scans, resulting in a bad segmentation in this area. The orange line indicating the RPE-Choroid boundary can be detected precisely. For this research study, the important information about the retina is located between the Vitreous-NFL and the RPE-Choroid boundary. Since on these two boundaries the algorithm worked the best, the overall results were highly satisfying.

For the calculation of the NFL-thickness, the NFL-GCL boundary has to be found. This boundary can be seen as a blue line in figure 4.6. It has its weak points in the vessel area, sometimes jumping away from the boundary, since the shadow of

the vessels disturbs the gradient based segmentation algorithm. Sometimes when the measured intensity of the NFL decreases on the edges, the blue line jumps down to the next layer boundary. This problem can be solved most of the time by increasing the vertical penalty to $w_v = 0.5$.

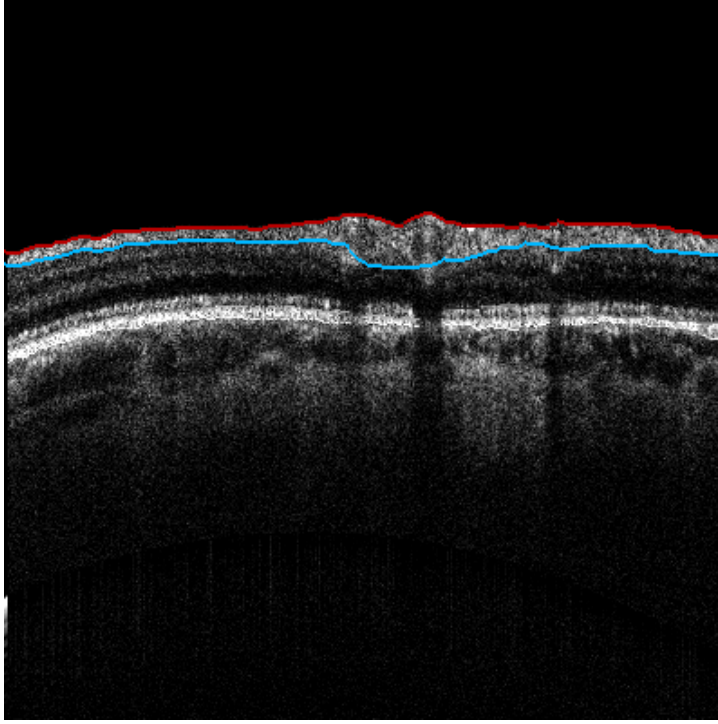


Figure 4.6: *Retinal layer segmentation on B-scan acquired with the 100kHz acquisition. The red line shows the vitreous - NFL boundary, while the blue line shows the NFL - GCL boundary as detected by the segmentation algorithm.*

In figure 4.7, the maximum projection of the angiography around the ONH can be seen before and after the layer segmentation. Since the noise above the retina is gone and the choroid is cut out, the image quality improves. Furthermore, the parameters for the 2D and 3D retinal perfusion are less influenced by noise.

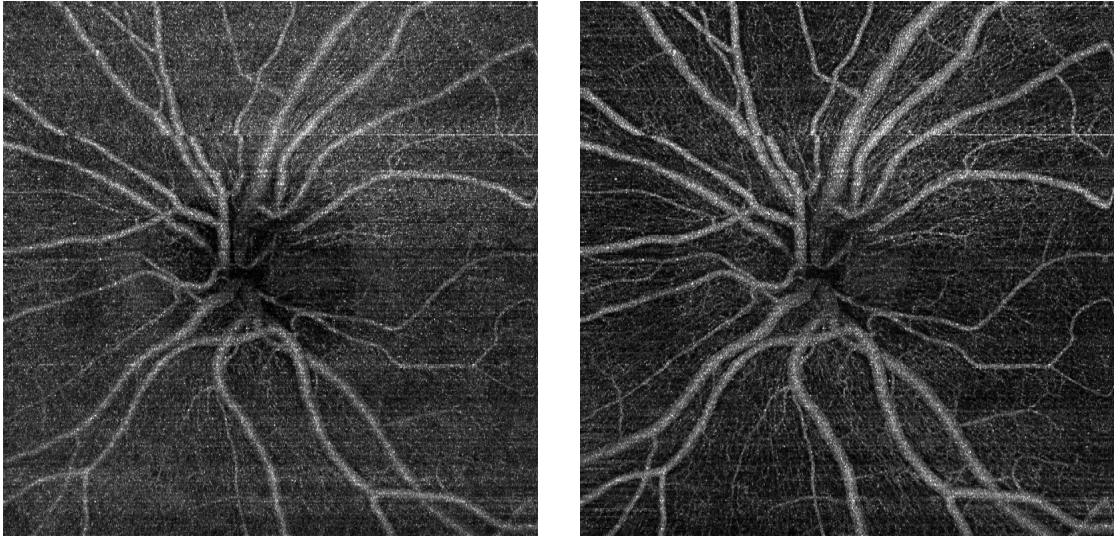


Figure 4.7: *En face maximum projection of the angiography gained with the 400kHz acquisition before (left) and after (right) the layer segmentation*

In figure 4.8 a comparison of the retinal layer segmentation between a B-scan acquired with the 100kHz acquisition and an angiography B-scan gained with the 400kHz acquisition can be seen.

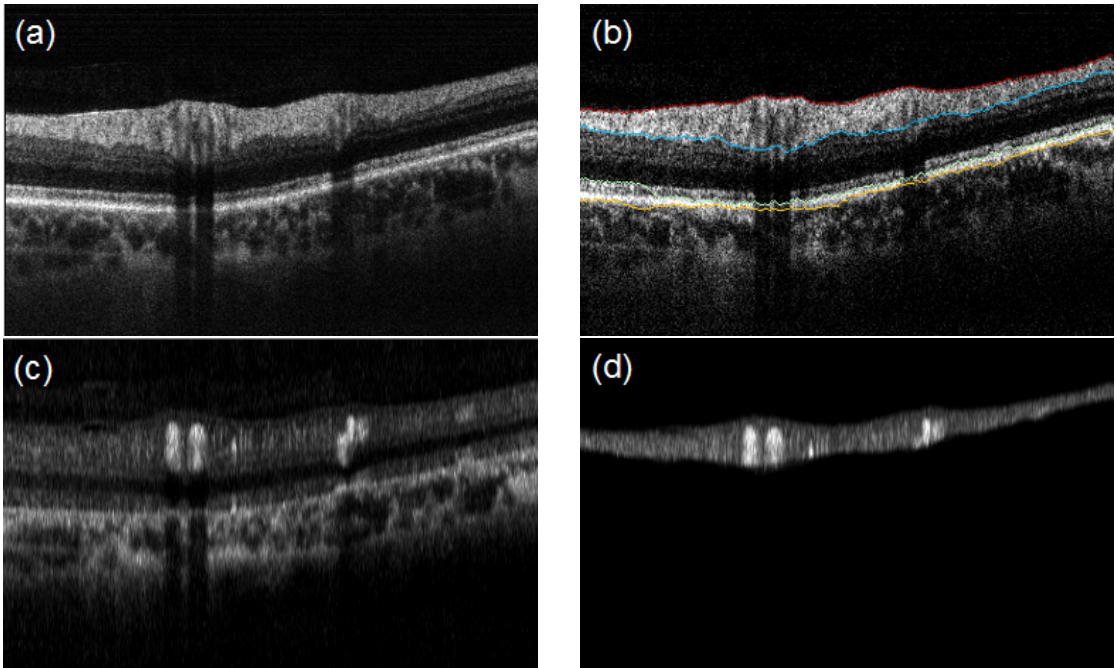


Figure 4.8: *(a) B-scan acquired with 100kHz acquisition, (b) Retinal layer segmentation on B-scan acquired with 100kHz acquisition, (c) B-scan acquired with 400kHz acquisition, (d) Mask of the NFL on the B-scan acquired with the 400kHz acquisition*

4.4 Major Vessel Segmentation

As has been described in chapter 3.3.4, the vessel segmentation algorithm is applied on the en face maximum projection of the angiography after the layer segmentation. It uses different combinations of intensity and cluster size threshold. Figure 4.9 shows the influence of the change of these parameters. The image on the left shows a good vessel segmentation with an intensity threshold high enough to get rid of the microvascular structure and a cluster size threshold low enough so that no vessels are cut out. Furthermore, the cluster size threshold has to be high enough to eliminate the outliers of the microvascular structure that have a higher intensity than the threshold. In the middle image, the loss of vessels can be observed when the cluster size threshold is too high. On the right side, the intensity threshold is not high enough to separate the vessels from the microvascular structure.

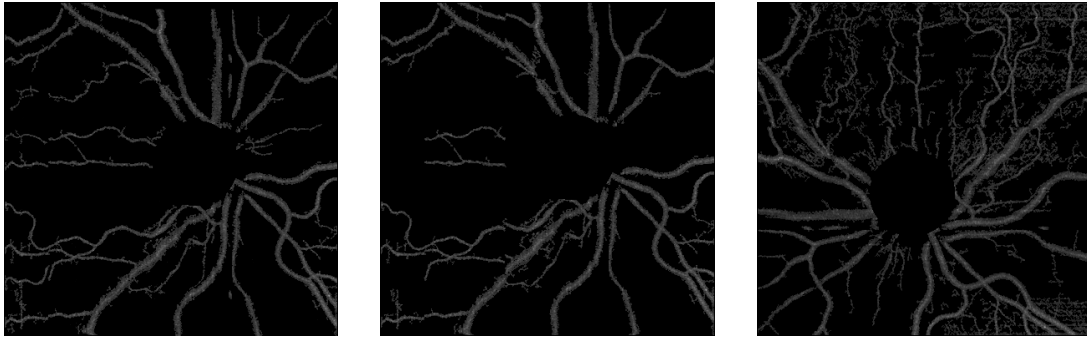


Figure 4.9: *Different vessel parameters for the major vessel segmentation:*
 Left: Intensity threshold: mean intensity value * 1.2, cluster size threshold: 30,
 Middle: Intensity threshold: mean intensity value * 1.2, cluster size threshold: 300,
 Right: Intensity threshold: mean intensity value * 1, cluster size threshold: 30.

The angiography used for this example can be seen in figure 4.10 on the left side. The image on the right side shows the final result without the ONH and the vessels, making it suitable for the calculation of the microvascular perfusion parameters.

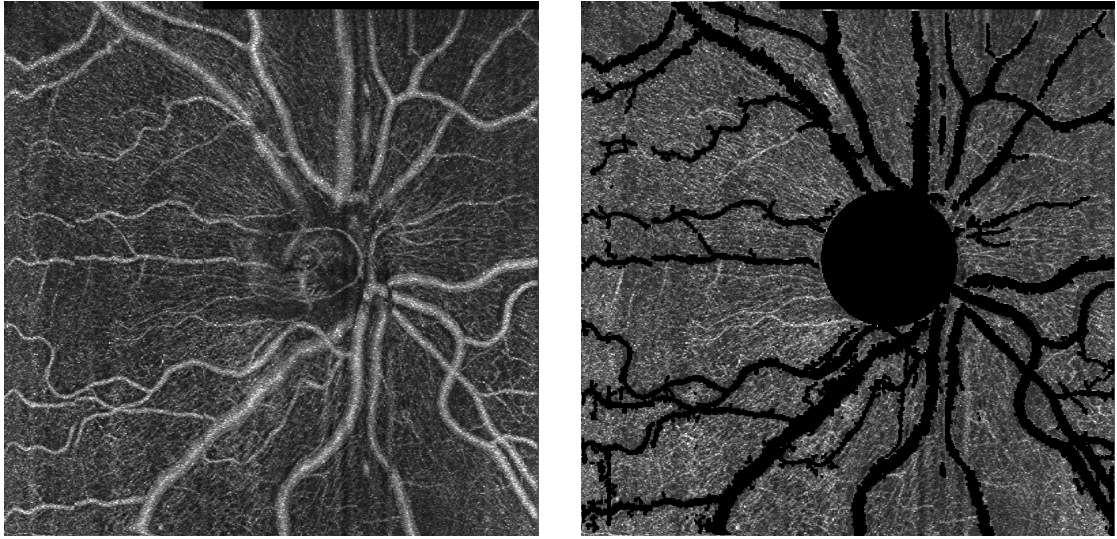


Figure 4.10: *En face maximum projection of the angiography gained with the 400kHz acquisition before (left) and after (right) the major vessel and ONH segmentation*

4.5 Retinal Perfusion

4.5.1 Comparison of NFL-thickness and retinal perfusion research study

The research study of Dr. Christoph Mitsch for which an algorithm was programmed along with the master thesis is still ongoing. This study examines whether there is a correlation between the NFL-thickness and retinal perfusion or not. The algorithm was tested on the data of participating patients that have already been imaged to see if the proof of principle can be verified with the available concept. The result of the tests on the existing data has shown that with the help of the algorithm, this issue can be examined. However, only five patients have been measured yet, which is not enough to present statistical results in this chapter. For the proof, only the segmented NFL was taken into account while the rest of the retina was excluded. Afterwards, the maximum projection of the remaining angiography was calculated and the major vessels and the ONH were excluded. After these exclusions, the image was subdivided in 6 divisions as is shown in figure 4.11. With the help of the layer segmentation algorithm, the average NFL-thickness can be calculated for each subdivision. Furthermore, the retinal perfusion parameters as described in 3.3.5 can be calculated for each subdivision and can be correlated with the corresponding NFL-thickness.

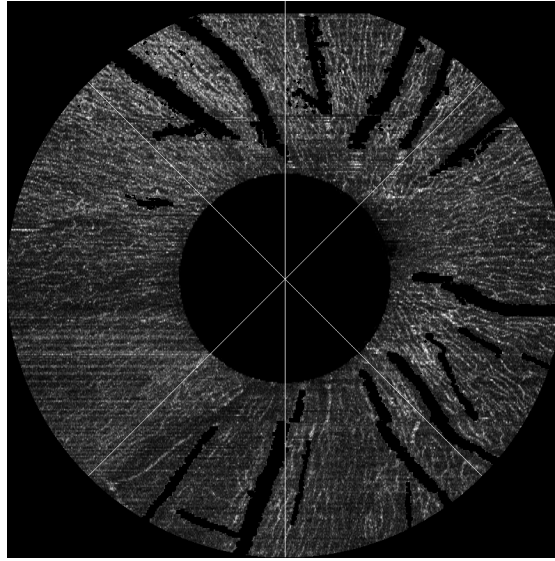


Figure 4.11: Cluster division for the research study by Dr. C. Mitsch

The microvascular perfusion parameters calculated for the shown example are listed in table 4.1. A comparison of the results of each division with the corresponding division in the figure shows that the microvascular perfusion parameters are reliable to reflect the actual situation. The nasal inferior, temporal inferior and temporal divisions with the least microvascular structure have the lowest values of the parameters, while the temporal superior and nasal superior divisions have a very dense microvascular structure with the highest parameter values.

Table 4.1: Microvascular perfusion parameters measured in six divisions: temporal superior (TS), nasal superior (NS), nasal (N), nasal inferior (NI), temporal inferior (TI), temporal (T)

Division	Flux	Vessel Area Density	Normalized Flux
TS	0.1150	0.9901	0.1161
NS	0.0947	0.9921	0.0955
N	0.0818	0.9882	0.0828
NI	0.0735	0.9927	0.0740
TI	0.0691	0.9930	0.0696
T	0.0749	0.9918	0.0755

Figure 4.12 shows the correlation between the calculated flux and the NFL-thickness, which was calculated from the segmented retinal layers (see chapter 3.3.2). The positive slope of the regression lines shows that the higher the flux, the higher the NFL-thickness. The only exception with a negative slope is patient 4.

4. Results and Discussion

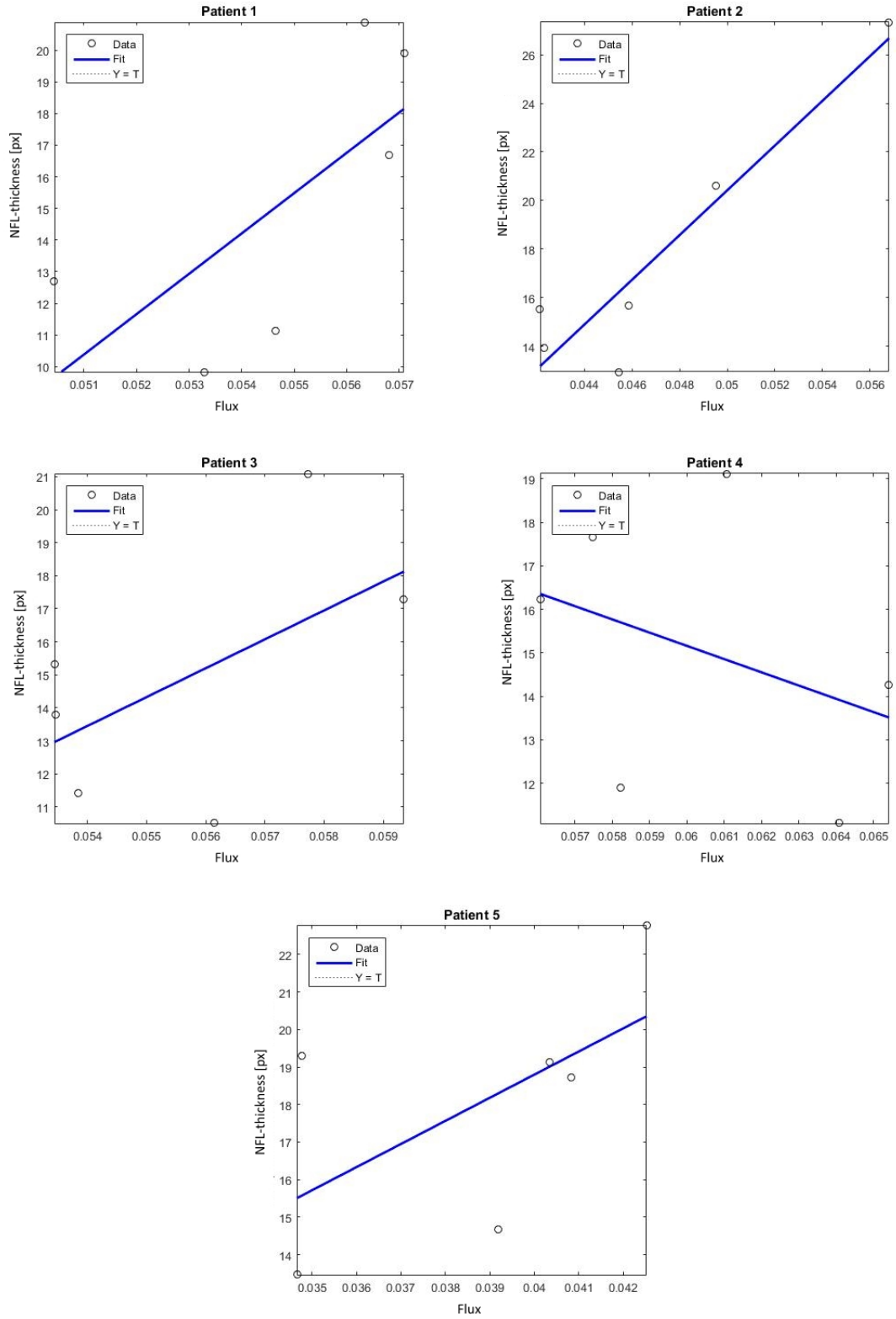


Figure 4.12: Correlation between the flux and the NFL-thickness calculated with the layer segmentation of the five imaged patients.

4.5.2 Retinal Oxygen Saturation and Microvascular Hemodynamic Parameters research study

Another algorithm was programmed for the study of Julia Hafner et al. [9]. The purpose of this study was to investigate if retinal oxygen saturation (SO₂) and microvascular hemodynamic parameters follow a distinct regional pattern in patients with diabetes but without diabetic retinopathy.

For this investigation, not only the ONH region but also the region around the fovea was imaged. The maximum projection of the angiography takes the retinal layers between the vitreous-NFL boundary and the RPE-choroid boundary into account. The images around the fovea were subdivided differently into four divisions (see figure 4.13 (left)) such as the images around the ONH (see figure 4.13 (right)). Afterwards, the flux was calculated for each division.



Figure 4.13: *Different cluster arrangements between the fovea images (left) and the ONH images (right).*

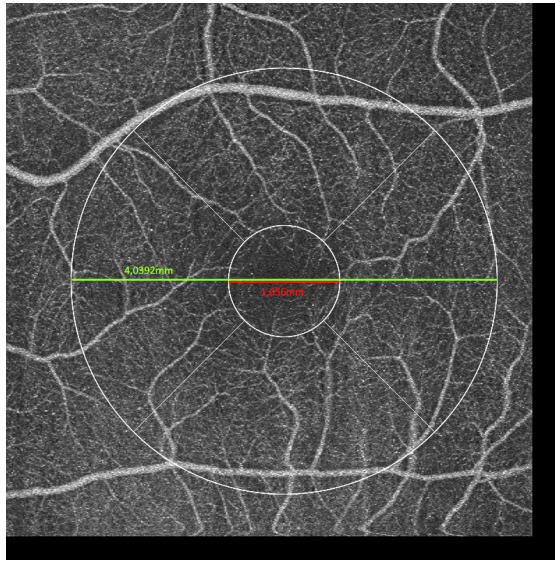


Figure 4.14: *Cluster parameter fovea*

The conclusion of this study is that the SO₂ differed significantly between the quadrants while the peripapillary flux followed an increasing trend from nasal to temporal, but demonstrated no significant regional variability.

5 Conclusion

The aim of this thesis was to support doctors in their search for biomarkers in the retina of the human eye. The discovery of biomarkers would help treat illnesses like glaucoma, age-related macular degeneration or diabetic retinopathy in an early stage or even before they occur. For that purpose, images of the retina were acquired from several patients participating in research studies with the help of a SS-OCT. The images were recorded by Laurin Ginner with the method he described in his thesis [6]. All patient data has been anonymized and no personal patient information was accessible for the master thesis. For this thesis, medical image processing algorithms were developed for these images of the retina.

The needs of the doctors for their research studies were to gather the flux, the vessel area density and the normalized flux of the retinal microvascular vessels, parameters that have been defined in chapter 3.3.5.

The first step to acquire these parameters was to process all the measured raw data into images. Because of the high number of measured patients, the already existing algorithms for this purpose had to be improved and modified in a way that allowed the processing to run automatically. Every patient from the research study was imaged up to six times to ensure that images with a proper quality, especially without motion artifacts, were available. In the first step, an algorithm programmed with the software LabView was used to gather the angiography of all measurements. After that, the maximum projection of the angiographies was calculated to estimate the image quality of the measurement. This is important since not all measurements of each patient could have been further processed because of the processing time and the high capacity of disk space needed for the storage of the data. To acquire the maximum projection, an image tool called ImageJ was used. Since every maximum projection needed to be processed manually with this tool, it would have been very time-consuming for a large amount of data. With the help of the software Matlab, an algorithm was written which could acquire the maximum projections of all needed data automatically. Once the measurement with the highest quality was found, the images obtained with 100kHz A-scan rate were processed with the help of an algorithm written in LabView. The images obtained with 100kHz were used for the retinal layer segmentation because they have a better depth resolution, making the segmentation more accurate. The algorithm programmed for the retinal layer segmentation was also coded with Matlab. It is a shortest path algorithm for which the cost function from the paper by Pratul P. Srinivasan et al. [14] was used (see chapter 3.3.2). With the help of the layer segmentation, the microvascular parameters were estimated in the desired layers for the research study only. Furthermore, algorithms were implemented for the segmentation of the ONH and the major vessels in order to get rid of the ONH and the major vessels. After that, the calculation of the parameters (flux, vessel area density and normalized flux) was applied to the microvascular structures only.

5. Conclusion

The vessel segmentation was based on a clustering method.

Overall these algorithms worked out very well. Therefore, the required results were provided satisfactorily for the research studies. However, the algorithms did not work out well on images with bad quality. Since images with bad quality are useless for research studies anyway, there was no need to focus on bad quality images in this thesis.

6 Outlook

Since the retinal layer segmentation has its weak points in the area around major vessels, a different approach for the segmentation could be considered. For this thesis the vessels are segmented with the help of the maximum projections. Thus only a 2D map of these vessels is gained. Another possibility for the vessel segmentation could use every B-scan from the data set, where the cross section of the vessels can be seen. The cross section of all vessels could be segmented with the help of an active contour (or snake) algorithm. This segmentation technique solves this task by minimizing an energy function. When all cross sections of each vessels in every B-scan are segmented, a full 3D map of the major vessels can be constructed. If the exact depth location of the vessels is known, this path of the layer segmentation can be skipped, which may lead to a better layer segmentation.

The used cluster arrangement for the calculations of the microvascular parameters as described in chapter 3.3.5 may not be best in terms of mathematics. Since it is investigated whether there is a correlation between these parameters and the NFL-thickness, it would be better if each cluster had the same size. With the used cluster arrangement, minima and maxima could be overseen. Since some clusters are relatively large, a cluster could contain a minimum and maximum, leading to an average value. To find out whether another correlation between the calculated perfusion parameters and the given parameters, such as O₂ saturation or NFL-thickness would change or not if the cluster arrangement is changed, the given parameters have to be measured with the same arrangement.

The usage of the algorithms stated in this thesis requires advanced knowledge of the softwares LabView and Matlab. If the coded algorithms were used for further research studies, it would be a great help to develop a user-friendly interface. This would give the doctors the possibility to gain the needed data by themselves, making it easier to realize their research studies. Furthermore, the image processing is highly time-consuming. To enhance the image processing speed, the algorithms should be reprogrammed in another programming language such as C++ and further use the fast processing speed of the GPU (graphics processing unit). It would be best if the processing speed reached a point where the angiography images can be observed close to real-time. This would allow to see if the imaging of a patient was successful or if too much motion or blinking had destroyed the measurement immediately after the recording.

References

- [1] **Marco Artico, Marialuisa Spoletini, Lorenzo Fumagalli, et al.** *Egas Moniz: 90 Years (1927–2017) from Cerebral Angiography*. Frontiers in Neuroanatomy, 2017.
- [2] **Nicole M. Artner.** *Lecture material: Einführung in die Musterkernnung, TU Vienna*. 2014–2015.
- [3] **C. Blatter, T. Klein, B. Grajciar, et al.** *Ultrahigh-speed non-invasive widefield angiography*. Journal Of Biomedical Optics.17(7):070505., 2012.
- [4] **Chieh-Li Chen, Karine D. Bojikian, Divakar Gupta, et al.** *Optic nerve head perfusion in normal eyes and eyes with glaucoma using optical coherence tomography-based microangiography*. Quantitative Imaging in Medicine and Surgery, 2016.
- [5] **Wolfgang Drexler and James G. Fujimoto.** *Optical Coherence Tomography*. Springer, 2008.
- [6] **Laurin Ginner.** *Improvement of High Speed Swept Source Optical Coherence Tomography for Optical Angiography*. 2016.
- [7] **Grehn.** *Augenheilkunde, 31. Auflage*. Springer, 2012.
- [8] **Manuel Guizar-Sicairos, Samuel T. Thurman, and James R. Fienup.** *Efficient subpixel image registration algorithms*. Opt. Lett. 33, 2008.
- [9] **Julia Hafner, Laurin Ginner, Sonja Karst, et al.** *Regional Patterns of Retinal Oxygen Saturation and Microvascular Hemodynamic Parameters Preceding Retinopathy in Patients With Type II Diabetes*. Invest Ophthalmol Vis Sci. 2017, 58:5541–5547. DOI:10.1167/iovs.17-22523, 2017.
- [10] **Georg Langs.** *Lecture material: Medizinische Bildverarbeitung, TU Vienna*. 2015.
- [11] **R. Leitgeb, C. K. Hitzenberger, and A. F. Fercher.** *Performance of fourier domain vs. time domain optical coherence tomography*. Optics Express. 11(8):889-94., 2003.
- [12] **Russell M. Levine, Alina Yang, Venkatesh Brahma, et al.** *Management of Blood Pressure in Patients with Glaucoma*. Springer Science+Business Media, DOI 10.1007/s11886-017-0927-x, 2017.
- [13] **Andrew M. Rollins and Joseph A. Izatt.** *Optimal interferometer designs for optical coherence tomography*. Opt Lett. 24(21):1484-6., 1999.

- [14] **Pratul P. Srinivasan, Stephanie J. Heflin, Joseph A. Izatt, et al.** *Automatic segmentation of up to ten layer boundaries in SD-OCT images of the mouse retina with and without missing layers due to pathology.* Biomedical Optics Express, 2014.
- [15] *Webside of MathWorks.* July 2, 2018. URL: <https://de.mathworks.com/help/>.
- [16] *Wikipedia.* URL: https://en.wikipedia.org/wiki/Human_eye#/media/File:Schematic_diagram_of_the_human_eye_en.svg.
- [17] **M. Wojtkowski, R. Leitgeb, T. Kowalczyk, et al.** *In vivo human retinal imaging by Fourier domain optical coherence tomography.* Journal of Biomedical Optics. 7(3):457-63., 2002.

List of figures

Fig. 2.1:	Comparison of resolution and imaging depth	6
Fig. 2.2:	Schematic OCT system	7
Fig. 2.3:	Basic principle of low-coherence interferometry	8
Fig. 2.4:	A-scan, B-scan and Tomogram	9
Fig. 2.5:	Basic principles of SD-OCT and SS-OCT	11
Fig. 2.6:	Schematic Michelson Interferometer	11
Fig. 2.7:	Model of a sample with discrete reflectors	12
Fig. 2.8:	Features of the spectral interferogram	15
Fig. 2.9:	Discrete reflector sample field reflectivity function and the result- ing A-scan from FD low-coherence interferometry	15
Fig. 2.10:	Detected signal at the photodetector	16
Fig. 2.11:	Axial resolution vs. bandwidth	16
Fig. 2.12:	Laser speckle	17
Fig. 2.13:	Shortest path problem with nodes, edges and weighting factors .	20
Fig. 2.14:	Image registration	21
Fig. 2.15:	Schematic diagram of the human eye	22
Fig. 2.16:	Schematic cut through the retina and the choroid	24
Fig. 2.17:	Retinal layers compared with OCT	24
Fig. 3.1:	Optical setup	27
Fig. 3.2:	Sweep structure of the Axsun laser	28
Fig. 3.3:	Split spectra approach	29
Fig. 3.4:	Different sweep structure examples	30
Fig. 3.5:	No remapping vs proper remapping	31
Fig. 3.6:	Matlab pixel coordinates	31
Fig. 3.7:	Matlab multidimensional Arrays	32
Fig. 3.8:	Segmentation layers	33
Fig. 4.1:	A result of the image registration algorithm	39
Fig. 4.2:	A result of displacement vectors	40
Fig. 4.3:	A result of the ONH segmentation	41
Fig. 4.4:	An example for an ONH mask	41
Fig. 4.5:	Result of a retinal layer segmentation on B-scan	42
Fig. 4.6:	Result of a retinal layer segmentation on B-scan for the NFL- thickness calculation	43
Fig. 4.7:	En face maximum projection of the angiography before and after layer segmentation	44
Fig. 4.8:	Retinal layer segmentation: Comparison of 100kHz image with angiography	44
Fig. 4.9:	Different vessel parameter for major vessel segmentation	45

Fig. 4.10: Result of a major vessel segmentation	46
Fig. 4.11: Cluster division for the research study by Dr. C. Mitsch	47
Fig. 4.12: Correlation between flux and NFL-thickness	48
Fig. 4.13: Cluster arrangement for retinal oxygen saturation research study	49
Fig. 4.14: Cluster parameter fovea	50

List of tables

Table 4.1: Microvascular perfusion parameters measured in six divisions: temporal superior (TS), nasal superior (NS), nasal (N), nasal inferior (NI), temporal inferior (TI), temporal (T)	47
--	----

List of equations

Eq. 2.1:	Intensity output proportional to the square of the total field . . .	8
Eq. 2.2:	Polychromatic plane wave	11
Eq. 2.3:	Series of N discrete real delta functions	12
Eq. 2.4:	Reflected beam from the sample arm	12
Eq. 2.5:	Reflected beam from the reference arm for discrete reflectors . . .	12
Eq. 2.6:	Reflected beam from the sample arm for discrete reflectors	13
Eq. 2.7:	Detector signal	13
Eq. 2.8:	Temporally invariant term of the detector signal	13
Eq. 2.9:	Normalized Gaussian function and its inverse Fourier transform .	13
Eq. 2.10:	Convention for Fourier transformation	13
Eq. 2.11:	Convolution property of Fourier transformation	13
Eq. 2.12:	Detector current	14
Eq. 2.13:	Axial resolution	16
Eq. 2.14:	Lateral resolution	17
Eq. 2.15:	Logarithmically scaled interferogram	18
Eq. 2.16:	Speckle variance	18
Eq. 2.17:	Thresholded speckle variances	18
Eq. 2.18:	Summation of speckle variance	18
Eq. 2.19:	Path costs for shortest path algorithm	19
Eq. 2.20:	Shortest path	19
Eq. 3.1:	Weighting factor used for the retinal layer segmentation	34
Eq. 3.2:	Flux	36
Eq. 3.3:	Vessel Area Density	37
Eq. 3.4:	Normalized Flux	37
Eq. 3.5:	Volume Flux	37
Eq. 3.6:	Vessel Volume Density	37
Eq. 3.7:	Normalized Volume Flux	38